

We thank the editor and two anonymous referees for reviewing our manuscript and providing us with constructive feedback. Below are our point-by-point responses to the referees' comments, followed by a revised manuscript showing all track changes made through the minor revision. Note referee's original comments are in italic and all line numbers are based on the revised manuscript

Reviewer #1:

General Comment: I appreciate the thorough response to my previous comments, especially with respect to discussion of pre-monsoon versus post-monsoon drought. I understand this is a nuanced distinction and that your model was not designed to identify snow- and rain-mediated differences in ecosystem fluxes. I have only a few remaining minor comments.

It's still unclear to me why the study considers ET and Reco but not GPP and/or NEE. i.e., two of the four main ecosystem carbon and water fluxes are included and the other two are excluded. What was the reason for this? I don't mean to be picky, and I'm certainly not suggesting that you re-do any analyses to include additional data, but readers will be wondering the same. Adding a sentence or two to justify/explain your rationale for your choice in the introduction, preferably early on, would go a long way toward setting appropriate expectations.

Response: We appreciate the reviewer for the summary of our work and feedbacks of our manuscript. We agree with the reviewer that GPP and NEE are important fluxes. In our previous response to reviewer comments, we developed HPM models to estimate NEE at several FLUXNET sites (Fig. A6). Based on those promising results, we think our proposed HPM framework has the capability to estimate NEE and GPP. In the revised manuscript, we have justified the rationale for our choice of R_{eco} (L26, L32-L37).

Table 1: You might consider adding a "Site name" column that would be helpful to readers that are familiar with these sites e.g., "Niwot Ridge" or similar for US-NRI. The units for precipitation are mislabeled as "(m)"; precipitation values could be rounded to the ones place.

Response: We have added a 'Site Name' column in Table 1 and corrected the unit for precipitation.

Line157: Change "closed" to close.

Response: We have made the necessary correction (L157).

Line401-417: This paragraph in particular would benefit from a grammar edit.

Response: We have edited the paragraph thoroughly and made necessary changes (L401-L415)

Reviewer #2:

General comment: This study uses a novel approach that combines process-based modeling and eddy covariance measurements with freely-available spatial datasets and machine learning to predict evaporation and respiration fluxes at the ecosystem scale. The input training data are meteorological data and remote sensing NDVI, which are linked to Measured (via eddy covariance, aka 'data HPM') or modeled (via Community Land Model, aka 'mechanistic HPM') DAILY et AND ECOSYSTEM RESPIRATION. The method used is a long short-term memory (LSTM) model – which is a type of recurrent neural network that has been used successfully for rainfall runoff and hydrological monitoring modeling. The authors demonstrated the use of both a data HPM and mechanistic HPM approach, and then used the latter method to model ET and Reco at several locations within the East River Watershed in southwestern

Colorado. The authors then relate the resulting modeled fluxes to changes in biome and year-to-year weather patterns. They conclude that HPM is a feasible method for estimating spatial and temporal patterns of ET and Reco, and I agree with them. This paper is written logically, with very few typos and needs just a bit of clarification (see my comments below). This paper is an interesting study on using data and tools available to us to address the need for spatially- and temporally-dense water and carbon fluxes, especially in mountainous landscapes. I am not an expert in neural network modeling, but I found the methods were not too difficult to follow.

Response: We thank the reviewer for the high-level summary of our work and positive remarks of our manuscript.

Line-by-line comments:

Line111: 'multi-model and multi-data approaches...'

Response: We have made the necessary change (L113)

Line223: Shouldn't 'CLM predictions' be added to the list of input features?

Response: We have made the necessary change (L223)

Line263: It is not clear to me why reconstruction of daily NDVI is necessary. Why can't the NDVI measurements be used with the gaps in time coverage? As long as there are accompanying meteorological measurements for that day, it should be fine. Please briefly add a statement justifying why it was necessary to gap-fill NDVI data and how many data points and the percentage of total NDVI data points were modeled instead of measured.

Response: Our current HPM configuration requires all input data to have the same temporal scale (i.e., daily), which is the main reason that we reconstruct daily NDVI time series (L264-L265). Thus, the NDVI reconstruction step is still necessary for HPM. Around 10% of the NDVI data points were measured given the 16-day revisit time of Landsat 8, which can be improved with ongoing advances in remote sensing.

Line501: 'These models were trained using and validated against eddy covariance...'

Response: We have made the necessary correction (L499).

A Deep-Learning Hybrid-Predictive-Modeling (HPM) Approach for Estimating Evapotranspiration and Ecosystem Respiration

Jiancong Chen¹, Baptiste Dafflon², Anh Phuong Tran^{2,3}, Nicola Falco², and Susan S. Hubbard²

¹Department of Civil and Environmental Engineering, University of California, Berkeley, CA, USA, ²Earth and Environmental Sciences Area, Lawrence Berkeley National Laboratory, Berkeley, CA, USA, ³Department of Water Resources Engineering and Technology, Water Resources Institute, 8, Phao Dai Lang, Dong Da, Hanoi, Vietnam

Abstract: Climate change is reshaping vulnerable ecosystems, leading to uncertain effects on ecosystem dynamics, including evapotranspiration (ET) and ecosystem respiration (R_{eco}). However, accurate estimation of ET and R_{eco} still remains challenging at sparsely monitored watersheds where data and field instrumentation are limited. In this study, we developed a hybrid predictive modeling approach (HPM) that integrates eddy covariance measurements, physically-based model simulation results, meteorological forcings, and remote sensing datasets to estimate ET and R_{eco} in high space-time resolution. HPM relies on a deep learning algorithm, long short-term memory (LSTM), and requires only air temperature, precipitation, radiation, normalized differences vegetation index (NDVI) and soil temperature (when available) as input variables. We tested and validated HPM estimation results in different climate regions and developed four use cases to demonstrate the applicability and variability of HPM at various FLUXNET sites and Rocky Mountain SNOTEL sites in Western North America. To test the limitations and performance of HPMs in mountainous watersheds, an expanded use case focused on the East River Watershed, Colorado, USA. The results indicate HPM is capable of identifying complicated interactions among meteorological forcings, ET, and R_{eco} variables, as well as providing reliable estimation of ET and R_{eco} across relevant spatiotemporal scales, even in challenging mountainous systems. The study documents that HPM increases our capability to estimate ET and R_{eco} and enhances process understanding at sparsely monitored watersheds.

1. Introduction:

Climate change has a profound influence on global and regional energy, water and carbon cycling, including evapotranspiration (ET), net ecosystem exchange (NEE), gross primary production (GPP) and ecosystem respiration (R_{eco}). ET is an important link between the water and energy cycles: dynamic changes in ET can affect precipitation, soil moisture, and surface temperature, leading to uncertain feedbacks in the environment (Jung et al., 2010; Seneviratne et al., 2006; Teuling et al., 2013). Thus, quantifying ET is particularly essential for improving our understanding of water and energy interactions as well as watershed responses to abrupt disturbances and gradual climate changes, which is critical for water resources management, agriculture, and other societal benefits (Anderson et al., 2012; Jung et al., 2010; Rungee et al., 2019; Viviroli et al., 2007; Viviroli and Weingartner, 2008). NEE, GPP and R_{eco} , which ~~represents~~represent the net carbon exchange, total carbon assimilation and total respiration in a specific ecosystem, ~~plays a~~respectively, play vital ~~roles~~roles in the response of terrestrial ecosystem to global climate change (Jung et al., 2017; Reichstein et al., 2005; Xu et al., 2004). ~~While~~Particularly, increases in R_{eco} may contribute to accelerating global warming through positive feedbacks to the atmosphere (Cox et al., 2000; Gao et al., 2017; IPCC, 2019; Suleau et al., 2011), estimating and monitoring R_{eco} over relevant spatiotemporal scales is challenging. As

38 described below, there are many different strategies for measuring and estimating ET and R_{eco} , each of which has
39 advantages and limitations. This study is motivated by the recognition that current methods cannot provide ET and
40 R_{eco} at space and time scales (e.g., daily) needed to improve prediction of changing terrestrial system behavior,
41 particularly in challenging mountainous watersheds.

42 Several ground-based approaches have been used to provide *in situ* estimates or measurements of ET and
43 R_{eco} . Ground-based flux chambers measure trace gases emitted from the land surface, which can be used to estimate
44 ET and R_{eco} (Livingston and Hutchinson, 1995; Pumpanen et al., 2004). The eddy covariance method uses a tower
45 with installed instruments to autonomously measure fluxes of trace gases between ecosystem and atmosphere
46 (Baldocchi, 2014; Wilson et al., 2001). ET is then calculated from the latent heat flux, and R_{eco} is calculated from the
47 net carbon fluxes using night-time or daytime partitioning approaches (van Gorsel et al., 2009; Lasslop et al., 2010;
48 Reichstein et al., 2005). The spatial footprint of obtained eddy covariance fluxes is on the order of hundreds of meters,
49 and the temporal resolution of the measurements ranges from hours to decades (Wilson et al., 2001). Tower-based *in*-
50 situ measurements of fluxes have been integrated into the global AmeriFlux (<http://ameriflux.lbl.gov/>) and FLUXNET
51 (<https://FLUXNET.fluxdata.org/>) networks. Eddy covariance towers are usually installed at valley bottoms of
52 mountainous watersheds (Strachan et al., 2016). Data from flux towers should also be used carefully as flux footprints
53 may vary significantly across sites and through time depending on site-specific information, turbulent states of the
54 atmosphere and underlying surface characteristics (Chu et al., 2021). Given the cost and efforts required to install and
55 maintain a flux tower, eddy covariance towers are typically sparse and may not capture complex fluxes at sites with
56 complex terrains, such as montane environments. Though measurements from a single flux tower may not capture
57 heterogeneity in ET and R_{eco} due to complex terrains, they can support the development of statistical or physical-based
58 models integrated with other types of data to provide ET and R_{eco} estimation as we describe herein.

59 Physically-based numerical models, which represent land-surface energy and water balance, have also been
60 used to estimate ET and R_{eco} (Tran et al., 2019; Williams et al., 2009), such as the Community Land Model (CLM,
61 Oleson et al., 2013). Performance of these models depends on the accuracy of inputs and parameters, such as soil type
62 and leaf area index, which can be difficult to obtain at a sufficiently high spatiotemporal resolution. The lack of
63 measurements to infer parameters needed for models often leads to large discrepancies between model-based and flux-
64 tower-based ET and R_{eco} estimates. Conceptual model uncertainty inherent in mechanistic models can also lead to ET
65 and R_{ECO} estimation uncertainty and errors. For example, Keenan et al. (2019) suggested that current terrestrial carbon
66 cycle models neglect inhibition of leaf respiration that occurs during daytime, which can result in a bias of up to 25 %.
67 Chang et al. (2018) suggested that process-based models may not represent transpiration accurately due to challenges
68 in simulating the uneven hydraulic distribution caused by complex terrain. Semi-analytical formulations are also
69 commonly used to estimate ET, including the Budyko framework and its extensions (Budyko, 1961; Greve et al., 2015;
70 Zhang et al., 2008); the Penman-Monteith's equation (Allen et al., 1998), and the Priestley-Taylor equation (Priestley
71 and Taylor, 1972). However, these conceptual uncertainties, in addition to data sparseness and data uncertainty, still
72 limit the applicability of these approaches.

73 Remote sensing products, such as Landsat imagery (Irons et al., 2012), Sentinel-2 (Main-Knorn et al., 2017)
74 and the moderate-resolution imaging spectroradiometer (MODIS, NASA, 2008), have also been integrated to estimate
75 ET and R_{eco} (Abatzoglou et al., 2014; Daggert et al., 2018; Mohanty et al., 2017; Paca et al., 2019). Ryu et al. (2011)
76 proposed the ‘Breathing Earth System Simulator’ approach, which integrates mechanistic models and MODIS data to
77 quantify ET and GPP with a spatial resolution of 1-5 km and a temporal resolution of 8 days. Ai et al. (2018) extracted
78 indices from the MODIS dataset—and used the rate-temperature curve and strong correlations between terrestrial
79 carbon exchange and air temperature to estimate R_{eco} at 1 km spatial resolution and 8-day temporal resolution. Ma et
80 al. (2018) developed a data fusion scheme that fused Landsat-like-scale datasets and MODIS data to estimate ET and
81 irrigation water efficiency at a spatial scale of ~100 meters. However, even though remote sensing data cover large
82 areas of the earth surface, they typically do not provide information over both high spatial and temporal resolution,
83 and data quality is subject to cloud conditions. For example, Landsat has average return periods of 16 days with a
84 spatial resolution of 30 m (visible and near-infrared), whereas MODIS has 1-2 days temporal resolution with a 250 m
85 or 1 km spatial resolution depending on the sensors. These resolutions are typically too coarse to enable exploration
86 of how aspects such as plant phenology, snowmelt, and rainfall influence water and energy dynamics of an ecosystem.

87 Combining machine-learning models with remote sensing products and meteorological inputs offers another
88 option for large-scale estimation of ET and R_{eco} . Remotely sensed data can be good proxies for plant productivity and
89 can be easily implemented into machine-learning models for ET and R_{ECO} estimation, such as for an enhanced
90 vegetation index, land surface water index and normalized differences vegetation index (NDVI) (Gao et al., 2015;
91 Jägermeyr et al., 2014; Migliavacca et al., 2015). Li and Xiao (2019) developed a data-driven model to estimate gross
92 primary production at a spatial and temporal resolution of 0.05° and 8 days. Berryman et al. (2018) demonstrated the
93 value of a Random Forest model to predict growing season soil respiration from subalpine forests in the Southern
94 Rocky Mountains ecoregion. Jung et al. (2009) developed a model tree ensemble approach to upscale FLUXNET data,
95 where they successfully estimated ET and GPP. Other methods have used support vector machines, artificial neural
96 networks, random forest, and piecewise regression (Bodesheim et al., 2018; Metzger et al., 2013; Xiao et al., 2014;
97 Xu et al., 2018). These models were trained with ground-measured flux observations and other variables, and then
98 applied to estimate ET over continental or global scales with remote sensing and meteorological inputs. Some of the
99 most important inputs include the enhanced vegetation index, aridity index, air temperature, and precipitation. The
100 spatiotemporal resolution of these approaches is constrained by the resolution of remote sensing products and
101 meteorological inputs. Additionally, parameters such as leaf area index, cloudiness, and the vegetation types required
102 by those models may not be available at the required resolution, accuracy or location. For example, in systems that
103 have significant elevation gradients, errors may occur when valley-based FLUXNET data are used for training and
104 then applied to hillslope or ridge ET and R_{eco} estimation.

105 Development of hybrid models that link direct measurements and/or mechanistic models with data-driven
106 methods can benefit ET and R_{eco} estimation (Reichstein et al., 2019). While remote sensing data that cover large
107 regions provide promise for informing models, quantitative interpretation of these data needed for input into
108 mechanistic models is still challenging (Reichstein et al., 2019). Physically based models can provide estimates of ET

109 and R_{eco} , but the estimate error can be high, owing to parametric, structural, and conceptual uncertainties as described
110 above. Hybrid data-driven frameworks are advantageous because they enable the integration of remote sensing
111 datasets, meteorological forcings, and mechanistic model outputs of ET and R_{eco} into one model. Machine-learning
112 approaches can then be applied to extract the spatiotemporal patterns for ET and R_{eco} prediction. The integration of
113 multi-model and multi-data [approaches](#) can increase our modeling capability to estimate ET and R_{eco} and enhance our
114 process understanding of ecosystem water and carbon cycling under climate change.

115 In this study, we developed a hybrid predictive modeling approach (HPM) to estimate daily ET and R_{ECO}
116 with easily acquired meteorological data (i.e., air temperature, precipitation and radiation) and remote sensing products
117 (i.e., NDVI). HPM is hybrid as it can flexibly integrate direct measurements from flux towers and/or physically-based
118 model results (e.g., CLM) and utilize deep learning long-short term memory recurrent neural network (LSTM) to
119 establish statistical relationships among fluxes, meteorological and remote sensing inputs. Once developed, the
120 corresponding HPM can be used as a modeling tool to estimate ET and R_{eco} over space and time. We developed four
121 use cases to demonstrate the applicability of HPM based on site-specific data and model availability. The remainder
122 of this paper is organized as follows. Section 2 mainly describes the sites considered in this study and how data were
123 acquired and processed. Section 3 presents the methodology of the HPM approach, followed by the results of various
124 use cases presented in Section 4. Discussion and conclusion are provided in Sections 5 and 6, respectively.

125 **2. Site Information, Data Acquisition and Processing**

126 The HPM method was tested using data from a range of different ecosystem types to explore its performance
127 under different conditions. We place a particular focus on mountainous sites, given their regional and global
128 importance yet challenges associated with ET and R_{eco} in these regions, as described above.

129 **2.1 FLUXNET Stations and Ecoregions**

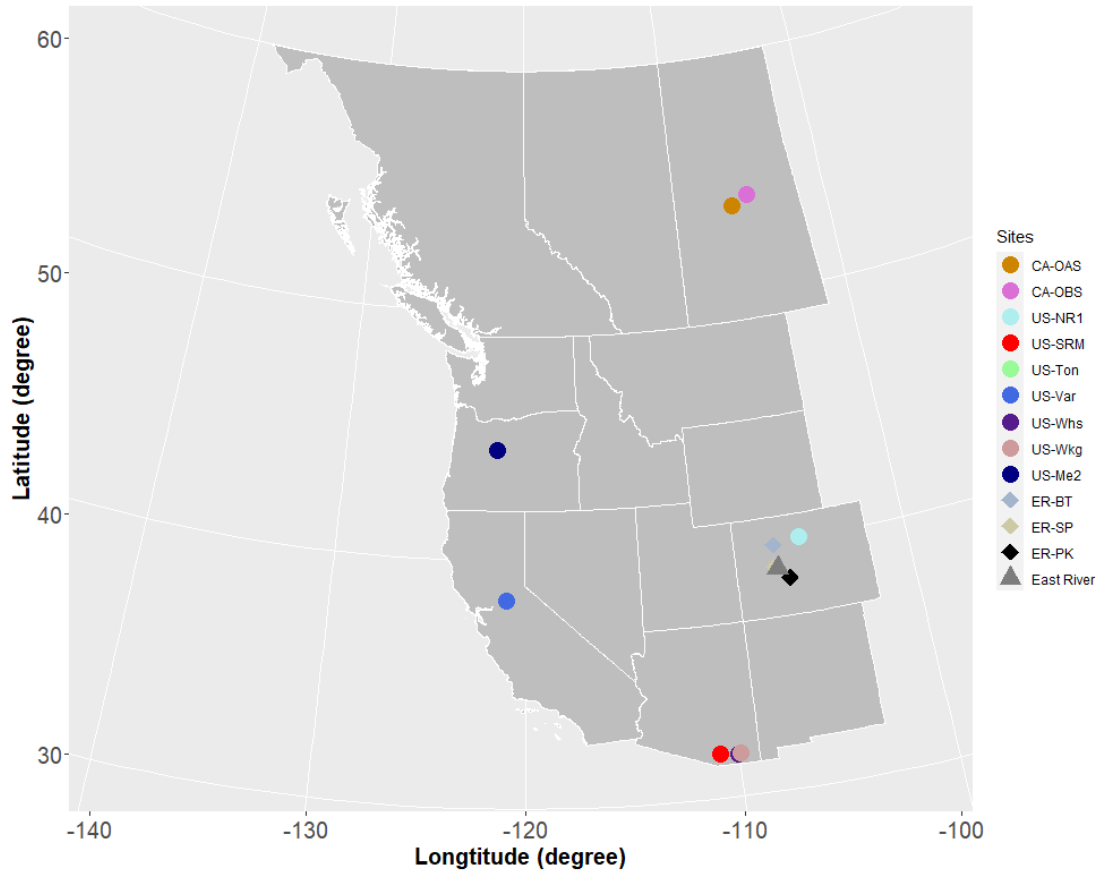
130 Nine FLUXNET stations, which cover a wide range of climate and elevations, were selected for this study
131 (Table 1 and Figure 1). These stations have elevations from 129 m (US-Var) to 3050 m (US-NR1), mean annual air
132 temperature from 0.34°C (CA-Oas) to 17.92°C (US-SRM), and mean annual precipitation from 320 mm (US-Whs) to
133 800 mm (US-NR1). These FLUXNET stations also cover a wide range of vegetation types (i.e., evergreen forest,
134 deciduous forest, and shrublands). As indicated by Hargrove et al. (2003), FLUXNET stations were maintained to
135 capture watershed dynamics at different ecoregions, which are areas that display recurring patterns of similar
136 combinations of soil, vegetation and landform characteristics (Omernik, 2004). Omernik & Griffith. (2014) delineated
137 the boundaries of ecoregions through pattern analysis that consider the spatial correlation of both physical and
138 biological factors (i.e., soils, physiography, vegetation, land use, geology and hydrology) in a hierarchical level.
139 FLUXNET stations considered in this study mainly locate in four unique ecoregions (Table 1). As is described below,
140 we developed local-scale (i.e., point scale) HPM that are representative for different ecoregions using data provided
141 at these FLUXNET stations to estimate ET and R_{ECO} , and validated the HPM estimates with measurements from
142 stations within the same ecoregion.

143 **2.2 SNOTEL Stations**

144 For reasons described below, we performed a deeper exploration of HPM performance within one of the
145 mountainous watershed sites (the East River Watershed of the Upper Colorado River Basin, USA), which is located
146 in the “western cordillera” ecoregion. At this site, we utilized meteorological forcings data from three snow telemetry
147 (SNOTEL) stations. These sites include the Butte (ER-BT, id: 380), Porphyry Creek (ER-PK, id: 701) and Schofield
148 Pass (ER-SP, id: 737) sites. A one-dimensional (vertical) CLM model was developed at these SNOTEL stations that
149 provides physically-model-based ET estimation (Tran et al., 2019). Table 1 summarizes the SNOTEL stations used in
150 this study and the corresponding climate characteristics. Figure 1 shows the geographical locations of FLUXNET and
151 SNOTEL stations selected in this study.

152 **Table 1. Summary of FLUXNET stations and SNOTEL stations information. * denotes SNOTEL stations and all others are FLUXNET stations. Dfc, Bsk, Csa represent**
 153 **subarctic or boreal climates, semi-arid climate, Mediterranean hot summer climates, respectively. ENF, DBF, WSA, GRA, and OSH represent evergreen needleleaf forest,**
 154 **deciduous broadleaf forests, woody savannas, grasslands, open shrubland, respectively. FLUXNET data were obtained from the FLUXNET2015 database.**

Site ID	Site Name	Latitude, Longitude	Elevation (m)	Mean Annual air temperature (°C)	Mean Annual Precipitation (mm)	Climate Koeppen	Vegetation IGBP	Ecoregion (Level II)	Period of Record
US-NR1	Niwot Ridge	(40.0329, -105.5464)	3050	1.5	800	Dfc	ENF	Western Cordillera	2000-2014
CA-Oas	Saskatchewan – Western Boreal, Mature Aspen	(53.6289, -106.1978)	530	0.34	428.53	Dfc	DBF	Boreal Plain	1997-2010
CA-Obs	Saskatchewan – Western Boreal, Mature Spruce	(53.9872, -105.1178)	628.94	0.79	405.6406	Dfc	ENF	Boreal Plain	1999-2010
US-SRM	Santa Rita Mesquite	(31.8214, -110.8661)	1120	17.92	380	Bsk	WSA	Western Sierra Madre Piedmont	2005-2015
US-Ton	Tonzi Ranch	(38.4316, -120.9660)	177	15.8	559	Csa	WSA	Mediterranean California	2002-2015
US-Var	Vaira Ranch - Ione	(38.4133, -120.9507)	129	15.8	559	Csa	GRA	Mediterranean California	2002-2015
US-Whs	Walnut Gulch Lucky Hills Shrub	(31.7438, -110.0522)	1370	17.6	320	Bsk	OSH	Western Sierra Madre Piedmont	2008-2015
US-Wkg	Walnut Gulch Kendall Grass	(31.7365, -109.9419)	1531	15.64	407	Bsk	GRA	Western Sierra Madre Piedmont	2005-2015
US-Me2	Metolius Mature Ponderosa Pine	(44.4523, -121.5574)	1253	6.28	523	Csb	ENF	Western Cordillera	2012-2015
ER-BT*	Butte (380)	(38.894, -106.945)	3096	2.38	821	Dfc	N/A	Western Cordillera	1995-2017
ER-SP*	Schofield Pass (737)	(39.02, -107.05)	3261	2.46	1064	Dfc	N/A	Western Cordillera	1995-2017
ER-PK*	Porphyry Creek (701)	(38.49, -106.34)	3280	1.97	574	Dfc	N/A	Western Cordillera	1995-2017



156
 157 **Figure 1. Location of sites considered in this study. Note: US-Ton and US-Var; US-Whs and US-Wkg are ~~closed~~close to**
 158 **each other. East River Watershed is located next to ER-BT. The white lines delineate Western US states and Canadian**
 159 **provinces. Circles represent FLUXNET sites, diamonds represent SNOTEL sites and triangle represents the East River**
 160 **Watershed.**

161 **2.3 East River Watershed Characteristics and Previous Analyses**

162 Data from the East River Watershed were used to explore how ET and R_{eco} dynamics estimated from the
 163 developed HPM vary with different vegetation and meteorological forcings. The East River Watershed is located
 164 northeast of the town of Crested Butte, Colorado. This watershed has an average elevation of 3266 m, with significant
 165 gradients in topography, hydrology, geomorphology, vegetation, and weather. The mean annual air temperature in the
 166 East River is $\sim 2.4^{\circ}\text{C}$, with average daily air temperatures of -7.6°C and 13.4°C in December and July respectively
 167 (Kakalia et al., 2020) and an average of 1200 mm yr^{-1} total precipitation (Hubbard et al., 2018). Consisting of
 168 montane, subalpine, and alpine life zones, each with distinctive vegetation biodiversity, the East River Watershed is a
 169 testbed for the US Department of Energy Watershed Function Scientific Focus Area Project, led by the Lawrence
 170 Berkeley National Laboratory (Hubbard et al., 2018). The project has acquired a range of datasets, including
 171 hydrological, biogeochemical, remote sensing, and geophysical datasets.

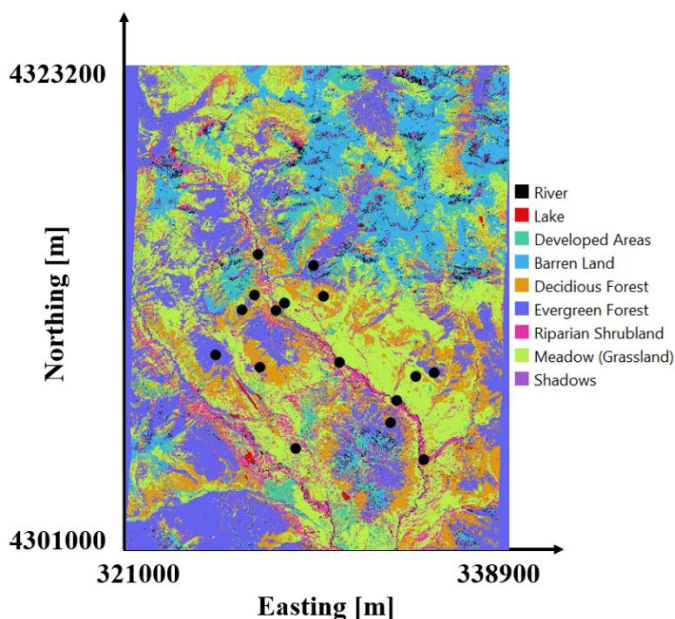
172 Recently completed studies at the East River Watershed were used in this study to inform HPM and to assess
 173 the results. For example, physically-model-based estimations of ET at this site (Tran et al., 2019) were used herein for

174 HPM development and validation. Falco et al. (2019) used machine-learning-based remote sensing methods to
 175 characterize the spatial distribution of vegetation types, slopes, and aspects within a hillslope at the East River
 176 Watershed, which were used with obtained HPM estimates to explore how vegetation heterogeneity influences ET
 177 and R_{ECO} dynamics. To perform this assessment, we computed the spatial distribution of vegetation types at watershed
 178 scale based on Falco et al. (2019). We evaluated manually and selected 16 locations within the East River Watershed
 179 having different vegetation types and slope aspects. These 16 locations were chosen to be at the center of vegetation
 180 patched and covered by one vegetation type. A summary of the locations is presented in Table 2; the spatial distribution
 181 of the locations is shown in Figure 2.

182 **Table 2: Location and vegetation types of East River Watershed sampling points (Figure 2)**

Easting (m)	Northing (m)	Vegetation Type	Aspect	Elevation (m)
327085	4309878	Deciduous Forest	South	2983
326288	4312504	Deciduous Forest	South	3177
330012	4313132	Deciduous Forest	North	3108
326854	4313192	Deciduous Forest	South	3098
328246	4312832	Meadow	South	3095
327010	4315059	Meadow	South	2790
328738	4306139	Meadow	North	2890
334270	4309465	Meadow	North	2929
333406.5	4308340	Riparian Shrubland	South	2760
327846	4312497	Riparian Shrubland	South	2723
334641	4305632	Riparian Shrubland	North	2740
330760	4310097	Riparian Shrubland	South	2855
329573	4314569	Evergreen Forest	South	3026
333106	4307313	Evergreen Forest	North	3102
325056	4310456	Evergreen Forest	South	2961
335141	4309614	Evergreen Forest	North	3131

183



184
 185 **Figure 2: Vegetation classification of the East River, CO Watershed from Falco et al. (2019). East River sites selected in**
 186 **this study are denoted by black circles.**

187 **2.4 Data Collection and Processing**

188 To enhance transferability of the developed HPM strategy to less intensively characterized watersheds, we
189 selected only “easy to measure” or “widely available” attributes, such as precipitation, air temperature, radiation and
190 NDVI, as inputs to the HTM model. Soil temperature was used when available. The data sources used for these inputs
191 include FLUXNET data (<https://fluxnet.fluxdata.org/>), SNOTEL data (<https://www.wcc.nrcs.usda.gov/snow/>) and
192 developed CLM model (Tran et al., 2019) at SNOTEL stations, DAYMET meteorological inputs (Thornton et al.,
193 2017) and remote sensing data from Landsat imageries (Irons et al., 2012). We identified some data gaps and erroneous
194 data (especially during winter seasons) for the ET estimates at US-NR1, which were cleaned following the procedures
195 presented in Rungee et al. (2019). At the three selected SNOTEL stations, air temperature data at these three SNOTEL
196 stations were processed following Oyler et al. (2015) and radiation data was obtained from DAYMET. CLM models
197 were generated following Tran et al. (2019) for the SNOTEL stations and US-NR1. At the East River Watershed sites,
198 data were obtained from DAYMET. NDVI time series were calculated from the red band and near-infrared band from
199 Landsat 5, 7 and 8 images at all sites. We used the cloud-scoring algorithm provided in the Google Earth Engine to
200 mask clouds in all retrieved data, only selecting the ones that had a simple cloud score below 20 to ensure data quality.
201 Given the different calibration sensors used in Landsat 5, 7, and 8, we also followed the processes described in Homer
202 et al. (2015) and Vogelmann et al. (2001) to keep NDVI computations consistent over time. Landsat satellites have a
203 return period of 16 days, and thus we performed a reconstruction of NDVI time series to obtain daily scale time data
204 (Section 3.2.2).

205 **3. Hybrid Predictive Modeling Framework**

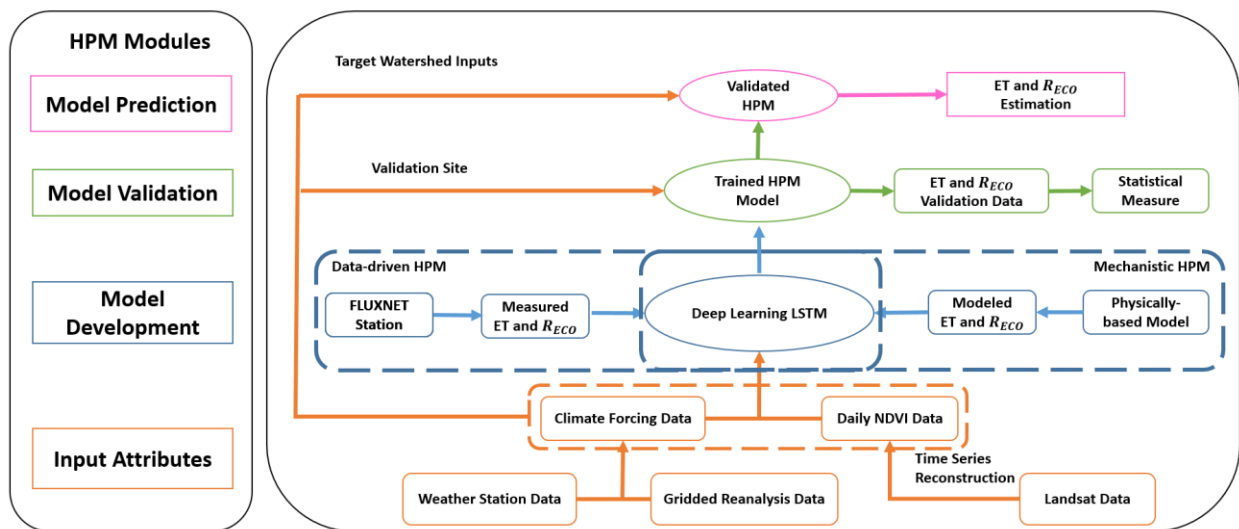
206 In this section, we illustrate the steps for building an HPM model for ET and R_{eco} estimation over time and
207 space. Figure 3 presents the general framework of HPM, which includes modules for data preprocessing, model
208 development, model validation, and predictive modeling.

209 **3.1 Model Framework**

210 HPM establishes relationships among meteorological forcings attributes, NDVI, ET and R_{eco} (Figure 3) using
211 deep-learning-based module (fully connected deep neural networks and long short-term memory recurrent neural
212 networks). Long short-term memory (LSTM, Hochreiter & Schmidhuber, 1997) is a type of recurrent neural network
213 (RNN) capable of learning temporal dependence without suffering from optimization difficulties (e.g., vanishing
214 errors). An LSTM layer consists of memory blocks and unique cell states that are controlled by three multiplicative
215 units, including the input, output and forget gates. These gates regulate the flow of information and decide which data
216 in a sequence is important to keep or throw away. Through the LSTM structure, even information from the earlier
217 time steps can make its way to later time steps, reducing the effects of short-term memory and thus capturing long-
218 term dependence. LSTM has been previously used to capture such dependencies between climate and environmental
219 data. For example, Kratzert et al. (2018) successfully used LSTM to learn the long-term dependencies in hydrological
220 data (e.g., storage effects within catchments, time lags between precipitation inputs and runoff generation) for rainfall-
221 runoff modeling. LSTM has also been used for gap filling in hydrological monitoring networks in the spatiotemporal
222 domain (Ren et al., 2019). More information about the LSTM-RNN method is provided by Olah (2015).

223 HPM modules include input attributes, model development, validation, and prediction. Based on data
 224 availability, input features are obtained from flux towers, CLM predictions, gridded meteorological data, and remote
 225 sensing data; all data are preprocessed for gap filling, smoothing, and updating. In the HPM model development
 226 module, individual HPM models can be trained in two different ways based on data availability: with data obtained
 227 from flux towers (“data-driven HPM”) or with outputs from physically-based models (“mechanistic HPM”). Seventy
 228 percent of these data are used for training LSTM to learn the interactions among input features, ET, and R_{eco} , until a
 229 pre-defined “stopping criteria” (e.g., root mean squared error, RMSE) is met, indicating subsequent training would
 230 lead to minimal improvement. In most models, the configuration of the neural networks includes a first LSTM layer
 231 with 50 units, a second LSTM layer with 25 units, and a dense layer with 8 units having L2 regularizers, and a final
 232 output dense layer. Dropout layers are also embedded in the model to prevent overfitting. There are 11600 and 7600
 233 parameters for the first and second LSTM layers; 208 and 9 for the first and second dense layers and no parameters
 234 for the dropout layers. Other configurations of networks may provide better estimation results; however, they are not
 235 assessed in this study as the proposed configuration already provide reasonable results.

236 In the validation module, we implemented a validation procedure that uses the remaining 30 % of the data to
 237 assess model performance. Estimation outputs from the trained HPM models are also compared with other ET and
 238 R_{eco} data obtained from other independent sites or mechanistic models within the same ecoregion. Statistical measures
 239 such as adjusted R^2 and mean absolute error (MAE) are computed to evaluate the performance of HPM models. In
 240 the predictive model module, meteorological forcings data and remote sensing data are processed at target sites of
 241 interest, and the validated HPM model is used to estimate ET and R_{eco} at these sites. ET and R_{eco} outputs estimated
 242 from HPM at sparsely monitored watersheds then provide alternative datasets for process understanding within the
 243 target watersheds.



244
 245 **Figure 3: Hybrid Predictive Model (HPM) Framework.** The HPM model mainly consists of four modules: **Input Attributes**,
 246 **Model Development**, **Model Validation** and **Model Prediction**, represented by rectangles with colors. Arrows represent the

247 linkages among different modules. Choices of data-driven HPM or mechanistic HPM depend on the ecoregion of target
248 watershed and data availability.

249 3.2 Feature Selection

250 At sparsely monitored watersheds, only weather reanalysis data and remote sensing data are commonly
251 available. Thus, we mainly considered air temperature, radiation, precipitation, vegetation indices (e.g., NDVI) and
252 variables inferred from these data as inputs for HPM. Soil temperature when available is used at FLUXNET sites.
253 Other key attributes that depend on depth and site-specific characteristics such as soil moisture and snow depth are
254 not used in current HPM models due to data availability.

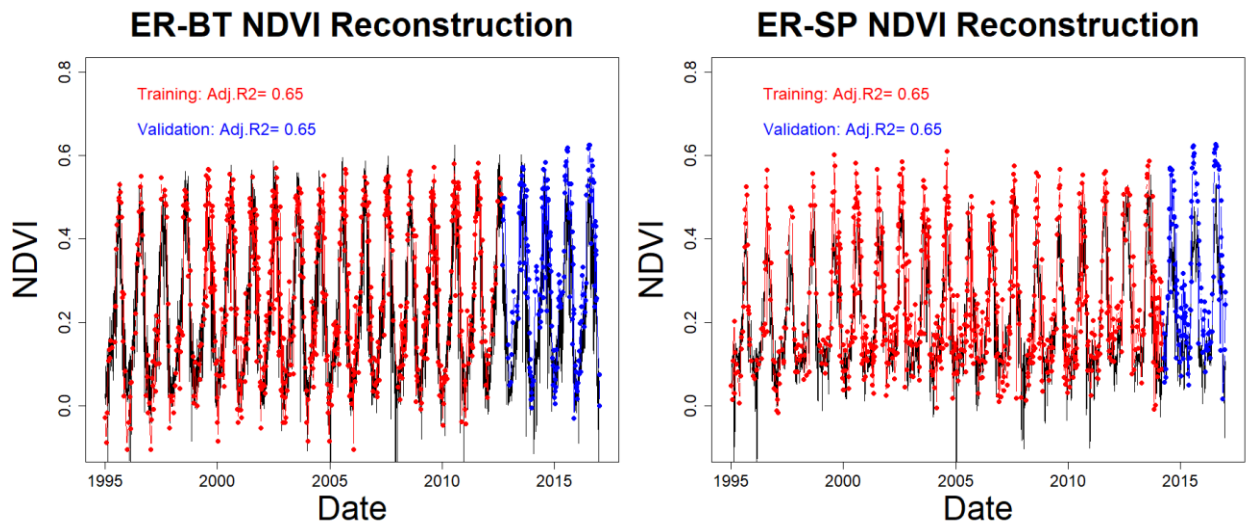
255 3.2.1 Snow information

256 In snow-influenced mountainous watersheds, we separated precipitation data into snow precipitation (when
257 air temperature < 0) and rainfall precipitation (when air temperature > 0), which is in line with what has been used in
258 hydrological models such as CLM (Oleson et al., 2013). Knowles et al. (2016) discovered a significant correlation
259 between day of peak snow accumulation, snowmelt and air temperature. To capture snow related dynamics (e.g.,
260 snowmelt), we constructed a categorical variable (*sn*) based on air and soil temperature thresholds. Note: this may not
261 be needed if snow data becomes available and at sites where snow is rarely present.

$$262 \quad sn = \begin{cases} 0, & \text{during snow accumulation; Air Temperature} < 0 \\ 1, & \text{during snow melting; Air Temperature} > 0 \text{ while Soil Temperature} \leq 0, \\ 2, & \text{no snow; Air Temperature and Soil Temperature} > 0 \end{cases} \quad (1)$$

263 3.2.2 Vegetation information

264 We reconstructed daily NDVI values based on meteorological forcing data (e.g., air temperature,
265 precipitation, radiation) using LSTM to increase the temporal coverage of NDVI- as the current HPM configuration
266 requires daily inputs. Figure 4 represents Landsat-derived NDVI and reconstructed NDVI values for two sites at the
267 East River, CO watershed: Butte (ER-BT), and Schofield Pass (ER-SP). Though not ideal, as satellites continue to
268 advance and more training data becomes available, the accuracy of NDVI temporal reconstruction is expected to
269 increase.



270

271 **Figure 4: Temporal reconstruction of NDVI at ER-BT (left) and ER-SP (right). Black lines represent reconstructed daily**
 272 **NDVI. Red points are used for training and blue points are used for validation**

273 3.3 Use Cases

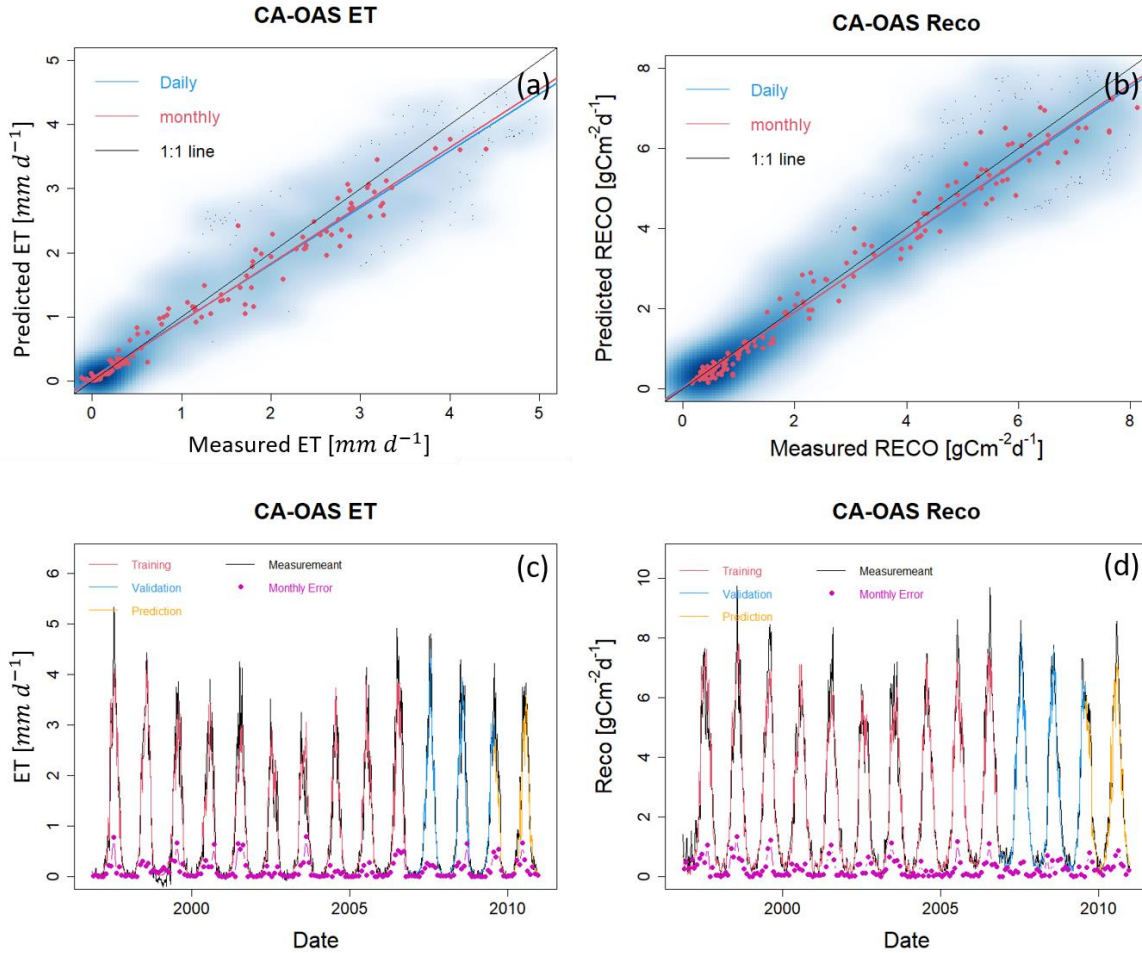
274 We developed four different use cases to demonstrate the applicability of HPMs based on site-specific data
 275 and model availability. Use case 1 focuses on ET and R_{eco} in the time domain, where a HPM is trained on direct
 276 measurements from flux tower. A 70%-20%-10% training-validation-prediction split of the data was used. These
 277 HPMs are useful for time series gap filling and future prediction. Use case 2 and use case 3 have emphasis on providing
 278 ET and R_{eco} over space, where use case 2 uses data-driven HPM and use case 3 utilizes mechanistic HPM. Data-driven
 279 HPM is trained with data from flux tower and mechanistic HPM is trained upon outputs from a mechanistic model
 280 (e.g., CLM). These HPMs are usually trained at well monitored watersheds where either flux data is available or data
 281 support the development of a mechanistic model. After training, these HPMs integrate meteorological and remote
 282 sensing inputs to provide ET and R_{eco} at target sparsely monitored watersheds within the same ecoregion. For both
 283 use case 2 and 3, we validated the HPM estimations against data from other sites within the same ecoregion. Use case
 284 4 focuses on the East River Watershed, where we demonstrate how HPM can increase our understanding of ecosystem
 285 fluxes and explore the limitations of HPM in mountainous watersheds. Use case 4 estimations were validated against
 286 data extracted from other studies.

287 4. Results

288 4.1 Use Case 1: ET and R_{ECO} Time Series Estimation with HPM Developed at FLUXNET Sites

289 Local HPMs were developed to estimate ET and R_{eco} using flux tower data obtained from FLUXNET sites
 290 listed in Table 1. At all FLUXNET sites, air temperature, precipitation, net radiation, NDVI and soil temperature were
 291 used. For US-NR1, CA-Oas and CA-Obs, sn is also included. The results, which are shown in Fig. 5, A1-A4 and
 292 Table 3, reveal that the HPM approach was effective for estimating ET and R_{eco} . The long-term trends in ET and R_{eco}
 293 are well captured by HPM. However, short-term fluctuations in ET and R_{eco} during the summer periods are also not
 294 well captured by HPM. For example, at US-Ton and US-Var, we observed an increasing discrepancy in summer month

295 ET and R_{eco} . This is mainly caused by insufficient training for summer extremes. At US-Me2, we observed significant
 296 increasing errors in the validation set, especially for R_{eco} that are caused by significant differences in raw data between
 297 2002-2010 (data used for training) and post-2011 (data used for validation).



298
 299 **Figure 5: ET and R_{eco} estimation with data from FLUXNET sites at CA-OAS. Panels (a) and (b) show the scatter plots of**
 300 **daily (blue) and monthly (red) ET and R_{eco} between HPM estimation and FLUXNET data. Darker blue clouds represent**
 301 **greater density of data points. Panels (c) and (d) present the daily HPM estimation of ET and R_{eco} separated by training,**
 302 **validation and prediction sets. Pink points depict monthly error between HPM estimation and FLUXNET data. Results for**
 303 **other sites are included in supplementary materials below (Fig. A1, A2, A3 and A4).**

304

Table 3: Statistical measures of HPM estimation of ET and R_{eco}

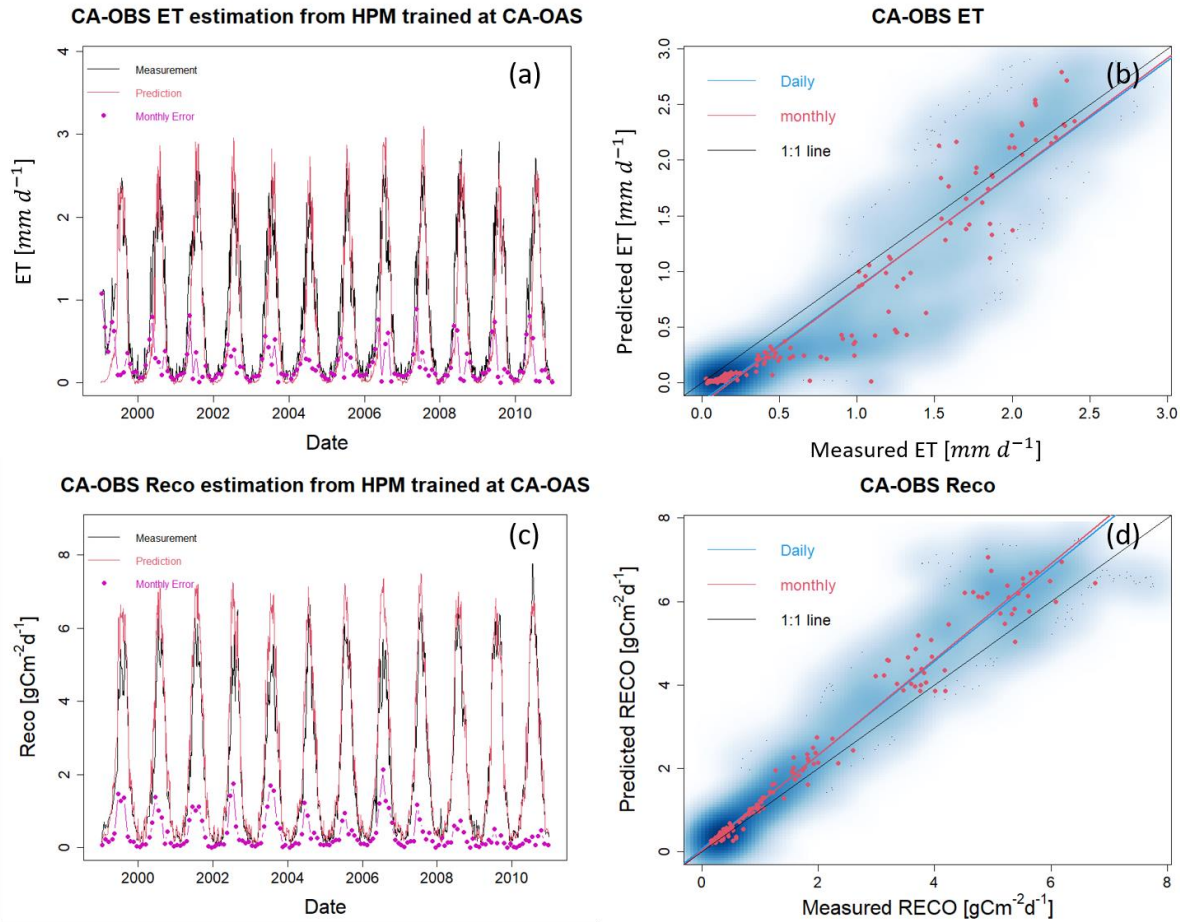
Site ID	Train MAE -ET [$mm\ d^{-1}$]	Test MAE -ET [$mm\ d^{-1}$]	Train Adj. R^2 - ET	Test Adj. R^2 - ET	Train MAE $-R_{eco}$ [$gCm^{-2}d^{-1}$]	Test MAE $-R_{eco}$ [$gCm^{-2}d^{-1}$]	Train Adj. R^2 $-R_{eco}$	Test Adj. R^2 $-R_{eco}$
US-NR1	0.19	0.11	0.95	0.98	0.33	0.18	0.91	0.98
CA-Oas	0.18	0.13	0.94	0.97	0.33	0.26	0.96	0.97
CA-Obs	0.12	0.09	0.95	0.96	0.29	0.25	0.96	0.97
US-SRM	0.22	0.17	0.92	0.94	0.24	0.19	0.80	0.87
US-Ton	0.22	0.17	0.92	0.94	0.43	0.36	0.76	0.82
US-Var	0.15	0.12	0.92	0.95	0.49	0.38	0.81	0.88

US-Whs	0.13	0.09	0.93	0.96	0.12	0.09	0.84	0.89
US-Wkg	0.19	0.15	0.87	0.91	0.18	0.15	0.85	0.91
US-Me2	0.36	0.43	0.81	0.75	0.75	0.83	0.88	0.85

305

306 **4.2 Use Case 2: Ecoregion-Based, Data-Driven HPM Model for ET and R_{ECO} Estimation**

307 In this section, we explored the use of a data-driven HPM trained with one FLUXNET station to estimate ET
308 and R_{eco} at other locations within the same ecoregion. Specifically, we developed HPM models at US-Ton, CA-Oas
309 and US-Wkg, and provided ET and R_{eco} estimations at US-Var, CA-Obs and US-Whs at three ecoregions, respectively.
310 Table 4 summarizes how we developed the data-driven HPM models for spatially distributed estimation of ET and
311 R_{eco} as well as the corresponding statistical summaries. Figures 6 and A5 present the time series of HPM-estimated
312 ET and R_{ECO} compared to measurements from flux towers. HPM estimation at US-Obs, US-Whs and US-Var
313 achieved an adjusted R^2 of 0.87, 0.88 and 0.91 for ET and 0.95, 0.70 and 0.78 for R_{ECO} , respectively. These results
314 show that HPM captures the seasonal and long-term dynamics of ET and R_{ECO} . However, at sites that experience
315 seasonally dry periods (e.g., US-Whs), prediction accuracy decreases during the peak growing season. Although the
316 prediction accuracy is not as high as Use Case 1 (Section 4.1), this use case demonstrates that HPM can learn the
317 complicated relationships between responses and features successfully, and that a local data-driven HPM can be used
318 to fuse with data from other subsites for long-term estimation of ET and R_{ECO} within the same ecoregions.



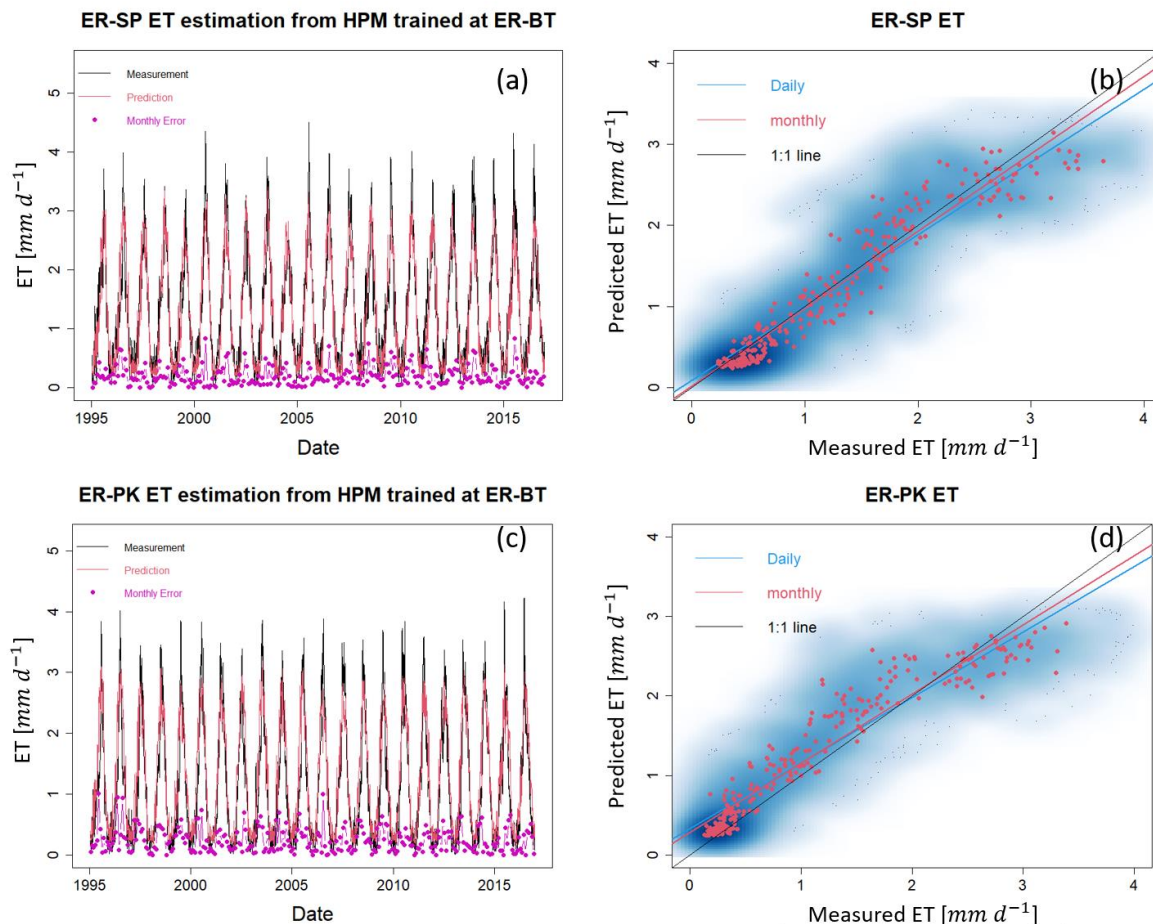
319
 320 **Figure 6. ET and R_{eco} estimation at CA-Obs using HPM trained at CA-Oas. Other sites are presented in Fig. A5.**

321 **4.3 Use Case 3: Ecoregion-Based, Mechanistic HPM Estimation of ET**

322 Mechanistic HPM, which is trained upon physically-based model simulations, provides an avenue for
 323 estimating fluxes in ecoregions where flux towers are not available. Consistent results between measured ET and
 324 CLM-estimated ET at US-NR1 (adjusted $R^2 = 0.88$; $k = 0.95$, Fig. S1) indicate independent CLM simulations can
 325 be effectively used to develop the mechanistic HPM. We applied mechanistic HPM trained with 1-Dimensional
 326 (vertical) CLM developed at ER-BT (Tran et al., 2019) to estimate ET at sites classified as part of the western
 327 Cordillera ecoregion (i.e., ER-SP, ER-PK and US-NR1). We then compared ET estimation from HPM to independent
 328 CLM-based ET estimations at ER-SP and ER-PK. Figure 7 shows a high consistency between HPM estimation and
 329 the validation data. For all scenarios, an adjusted R^2 of 0.8 or greater is observed (Table 4), which strongly indicates
 330 that mechanistic HPM can provide accurate ET estimation at sites of similar ecoregions. These results suggest the
 331 broad applicability of mechanistic HPM to estimate ET based on ecoregion characteristics. This approach is expected
 332 to be particularly useful for regions where flux towers are difficult to install or where measured fluxes are not
 333 representative of the landscape, such as in mountainous watersheds.

334 **Table 4. Statistical summary of HPM estimation over space with FLUXNET sites and SNOTEL stations with CLM**

Target Site	Training Site	Level II Ecoregion	ET MSE (monthly) [$mm d^{-1}$]	ET Adj. R^2	R_{eco} MSE(monthly) [$gCm^{-2}d^{-1}$]	R_{eco} Adj. R^2
CA-Obs	CA-Oas	Boreal Plain	0.39	0.88	0.36	0.97
US-Var	US-Ton	Mediterranean California	0.34	0.70	0.67	0.70
US-Whs	US-Wkg	Western Serra Madre Piedmont	0.13	0.94	0.17	0.85
ER-SP	ER-BT	Western Cordillera	0.20	0.92	-	-
ER-PK	ER-BT	Western Cordillera	0.24	0.90	-	-

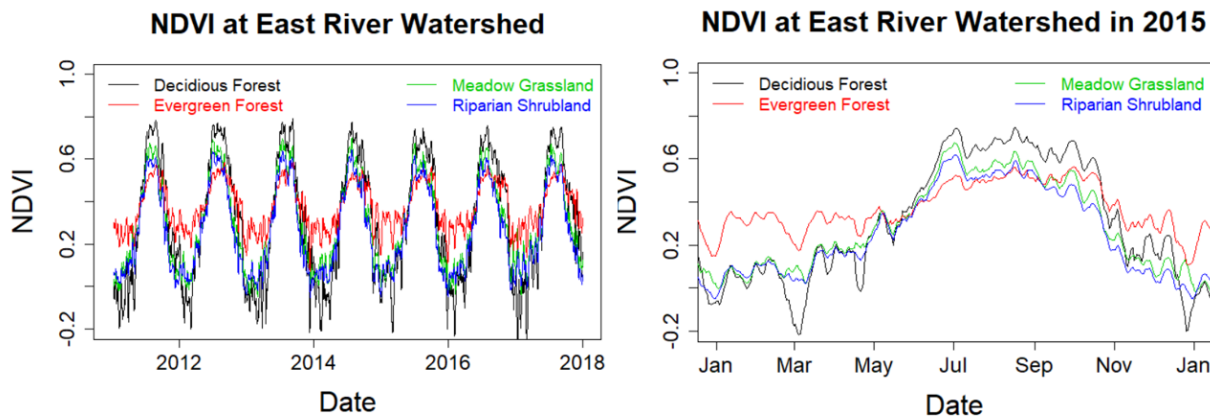


335
 336 **Figure 7.** HPMs trained with CLM simulation at ER-BT are used to estimate ET at ER-SP and ER-PK. Panels (a) and (c)
 337 display the time series of HPM estimation of ET (red lines), and independent CLM estimation at ER-SP and ER-PK. Panels
 338 (b) and (d) show the scatter plots of daily (blue) and monthly (red) ET at these sites. Darker blue clouds represent greater
 339 density of data points.

340 **4.4 Use Case 4: HPM approach improved our prediction capability and process understanding at the East**
 341 **River Watershed**

342 With the proposed HPM approach (e.g., mechanistic HPM), we were able to estimate ET and R_{eco} at selected
 343 locations at the East River Watershed, CO, USA with only meteorological forcings and remote sensing data. Our
 344 estimations are comparable to other independent studies, such as Mu et al. (2013) (Fig. S2) and Berryman et al. (2018).
 345 HPM estimations enhanced our understanding of watershed processes and enabled us to explore the limitations in the
 346 developed HPM approach especially at mountainous watersheds.

347 Physiology differences among vegetation types and dynamic changes in meteorological conditions were well
 348 captured by input features and HPM at the East River Watershed. Not surprisingly, the reconstructed NDVI indicated
 349 that deciduous forests have the highest peak NDVI followed by grasslands, shrublands and evergreen forests whereas
 350 annual variation of NDVI in evergreen forests is smaller than the other vegetation types (Fig. 8). Year 2012 is regarded
 351 as a fore-summer drought year with earlier than normal snowmelt, and year 2015 is regarded as a normal water year.
 352 The Palmer drought severity index (PDSI) is -5.2 and -1.5 for June and -4.6 and 1.1 for August in 2012 and 2015,
 353 respectively. Dynamic changes in meteorological conditions between 2012 and 2015 were also reflected in the
 354 reconstructed NDVI time series. We observed an earlier rise of NDVI in 2012: March, April and May mean NDVI
 355 values for deciduous forest sites are 0.07, 0.2 and 0.37 compared to 0.06, 0.15 and 0.33 in 2015. Similar trends were
 356 observed for other vegetation types during spring months as well. NDVI values remain high during the peak growing
 357 season (deciduous forest > grassland > shrubland > evergreen forest) for both 2012 and 2015. However, we observed
 358 NDVI declines for grasslands and shrublands since August in 2012 but not until September in 2015. During autumn
 359 periods, NDVI declines significantly following the sharp decline in radiation.

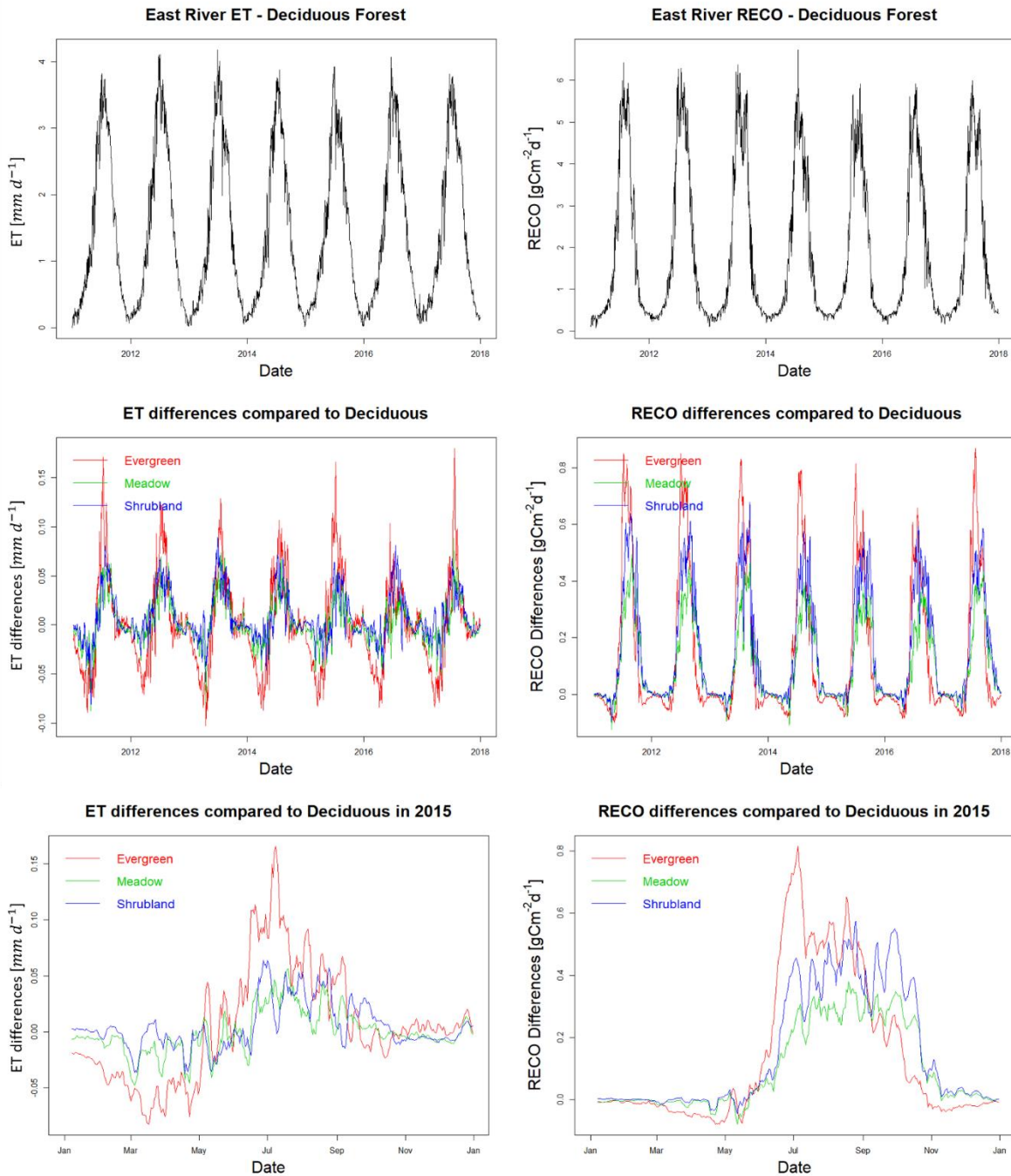


360
 361 **Figure 8: Reconstructed NDVI time series at selected locations in the East River Watershed for 2011 to 2018 (panel a) and**
 362 **for 2015 (panel b, normal water year). Black, red, green, and blue lines represent the time series of NDVI for deciduous**
 363 **forests, meadow grasslands, evergreen forests and riparian shrubland, respectively.**

364 HPM-estimated ET and R_{eco} also show different dynamics with different vegetation types and meteorological
 365 conditions. Figure 9a and 9b present the time series of estimated ET and R_{eco} associated with deciduous forests,
 366 respectively. Figure 9c and 9d present the ET and R_{eco} differences between deciduous forests sites and evergreen
 367 forests, shrublands and grasslands. Before peak growing season, evergreen forests have the greatest ET and R_{eco}
 368 compared to the other vegetation types. ET of evergreen forests is about 10% greater than deciduous forests, whereas
 369 ET of deciduous forests during peak growing season is greater than evergreen forests, shrublands and meadows. After
 370 growing season, the NDVI of deciduous forests is less than 0.2 (loss of leaves) compared to the NDVI of evergreen
 371 forests. Before peak growing season, R_{eco} of evergreen forests is slightly greater than deciduous forests, meadow
 372 grasslands and shrublands. During peak growing season, we observed largest R_{eco} for deciduous forests sites (~ 6
 373 $gCm^{-2}d^{-1}$) followed by meadows, shrublands and evergreen forests. R_{eco} of deciduous forests is around 17 % greater

374 than R_{eco} of evergreen forests. However, we did not observe significant differences in annual ET among these four
375 vegetation types (e.g., DF: 535 to 573 mm, MS: 534 to 570 mm, RS: 532 to 567 mm and EF: 532 to 569 mm across 7
376 years in this study). Total annual R_{eco} of deciduous forests is greater than the other vegetation types (DF1: 642 to 698
377 gCm^{-2} , MS1: 588 to 636 gCm^{-2} , RS1: 589 to 636 gCm^{-2} and EF1: 592 to 639 gCm^{-2}). These results indicate HPM
378 R_{eco} models are sensitive to vegetation types and HPM ET models are mostly constrained by meteorological conditions.

379 Considering the inter-annual variability in meteorological forcings, we further selected year 2014 (large snow
380 precipitation ~ 587 mm but small rain precipitation ~ 275 mm) in addition to 2012 (drought year) and 2015 (small
381 snow precipitation ~ 383 mm and large rain precipitation ~ 477 mm) to test HPM performance. As HPM does not
382 have the capability to identify snow and monsoon precipitation's contribution to fluxes, we separated annual ET and
383 R_{eco} into pre-June (January-June) and post-July (July-December) to quantify the contribution from snow and monsoon.
384 Earlier snowmelt that occurred in 2012 boosted spring ET and R_{eco} and we observed larger March-mean ET and R_{eco}
385 compared to 2014 and 2015 that are characterized by later snowmelt. Occurrences of fore-summer drought in 2012
386 led to moisture limiting conditions, resulting in large fluctuations of ET and R_{eco} during May and June. ET fluctuated
387 from 2.9 to 1.9 $mm d^{-1}$ during late May, and 3.53 to 2.6 $mm d^{-1}$ during early June. However, early occurrence of
388 monsoon in 2012 led to a peak ET in early July. Due to late snowmelt, ET did not significantly fluctuate in 2014 and
389 2015. However, peak ET shifted towards late July in 2014. Regarding R_{eco} dynamics, fore-summer drought conditions
390 led to variations in R_{eco} from ~ 4 to 6 $gCm^{-2} d^{-1}$ in 2012. In 2014, we observed more steady increase of R_{eco} during
391 the early and peak growing seasons. For late-summer and autumn months (August – October), ET decreased steadily
392 in all three years regardless of monsoon precipitation inputs, following the significant decline in radiation. Pre-June
393 ET and R_{eco} (255mm and 217 $gCm^{-2} d^{-1}$) were both greater in 2012 compared to 2014 (223 mm and
394 178 $gCm^{-2} d^{-1}$) and 2015 (230 mm and 197 $gCm^{-2} d^{-1}$) in deciduous forests. While there were no significant
395 differences in post-July ET among the three years (318, 316 and 306 mm), 2012 was the highest. Within deciduous
396 forests and annually over 2012, 2014 and 2015, ET was 573 mm, 539 mm and 536 mm and R_{eco} was 698 gCm^{-2} ,
397 642 gCm^{-2} and 652 gCm^{-2} , respectively. . Similar trends were observed for other vegetation types.

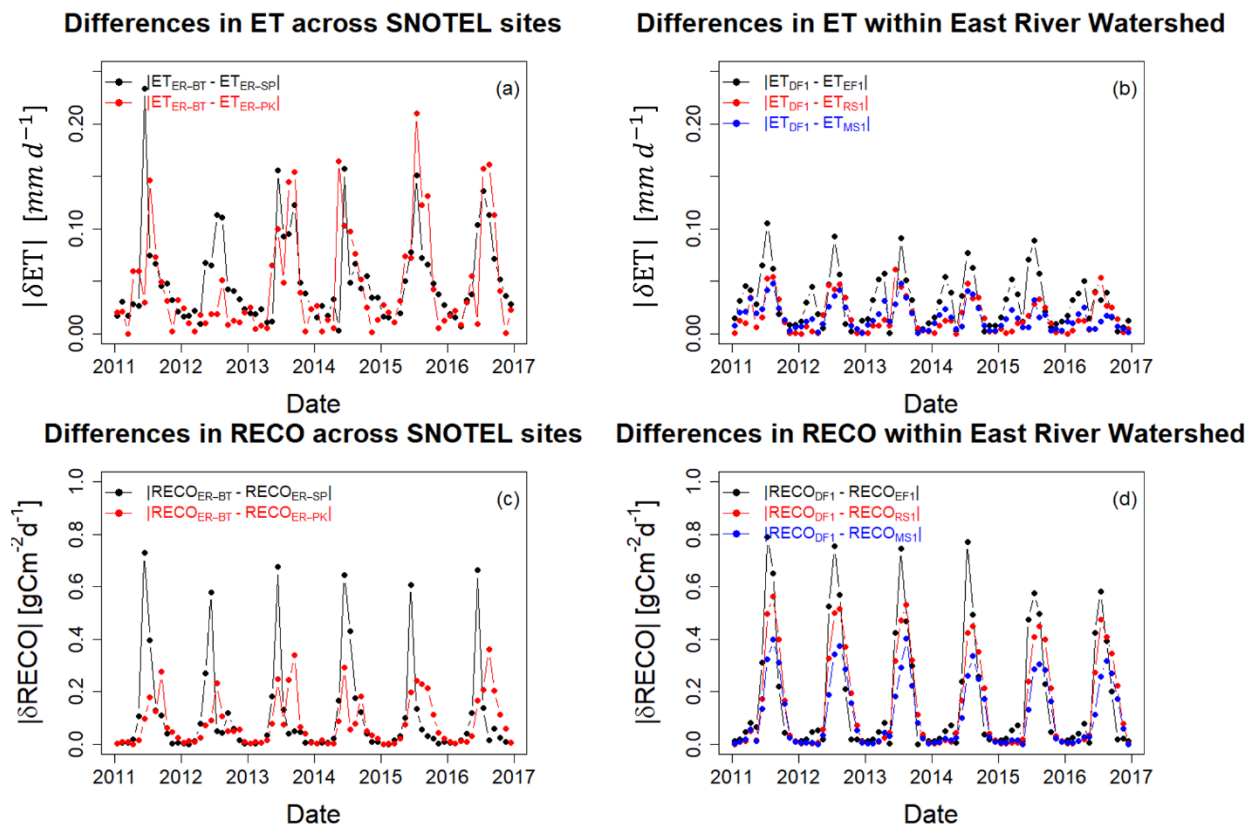


398

399 **Figure 9: ET (a) and R_{eco} (b) estimation for the deciduous forest site DF1 at the East River Watershed. Panels (c) and (d)**
 400 **show the differences in ET and R_{eco} among various vegetation types and deciduous forest. Red, green, and blue lines**
 401 **represent the differences in evergreen forest, meadow, and riparian shrubland compared to deciduous forest. Panels (e)**
 402 **and (f) zoom into 2015 to better display seasonal variations.**

403 Though HPM estimations allowed us to explore differences in ET and R_{eco} across vegetation types and
 404 meteorological forcings heterogeneity, it is necessary to investigate the limitations of the HPM approach. Figure 10
 405 shows the absolute value of monthly mean difference in ET (Fig. 10a and Fig. 10b) and R_{eco} (Fig. 10c and Fig. 10d)

406 across SNOTEL stations (ER-BT, ER-SP and ER-PK) and within selected East River locations. We observed greater
 407 differences in air temperature and radiation at the SNOTEL sites ~~and but~~ very small differences at the East River sites
 408 (Figure S4). Differences in June air temperature ~~differences~~ among SNOTEL sites were occasionally over $3\text{ }^{\circ}\text{C}$, while
 409 ~~the~~-DAYMET data from the East River ~~rarely revealed~~indicated a $0.2\text{ }^{\circ}\text{C}$ differences. In addition, a $\sim 80\text{ }W\text{ }m^{-2}$ of
 410 radiation differences was observed with SNOTEL data ~~whereas radiation differences stays around~~ compared to 30
 411 $W\text{ }m^{-2}$ for East River sites. ~~Correspondingly, we observed~~ As a result, ET differences across SNOTEL stations are
 412 2.5 times greater than differences ~~in ET across SNOTEL stations compared to the sites within~~ observed at the East
 413 River ~~watershed. We observed~~ locations. A similar level of differences (around $0.8\text{ }gCm^{-2}$) was observed in R_{eco}
 414 within the East River Watershed and across SNOTEL stations. ~~Landsat data enabled us to capture NDVI differences~~
 415 ~~at these sites, but we have identified~~ These results suggest the insufficient resolution of input meteorological forcing
 416 data at the East River sites. ~~These results indicate~~ have large uncertainties ~~in meteorological forcing attributes (e.g.,~~
 417 ~~radiation and air temperature) can, which~~ have a huge significant influence over HPM ET ~~estimation~~ and HPM R_{eco}
 418 ~~model is more sensitive to NDVI datasets estimations~~. If high resolution meteorological data becomes available for
 419 the East River watershed, we believe the HPM approach can better capture heterogeneities in ET and R_{eco} at the East
 420 River watershed and better distinguish the roles of meteorological forcing and vegetation heterogeneity on ET and
 421 R_{eco} distribution.



422
 423 **Figure 10. Absolute differences in monthly mean ET and R_{eco} across SNOTEL stations and within East River Watershed.**
 424 **Panels (a) and (c) describe the absolute differences in monthly mean ET and R_{eco} between ER-BT, ER-SP, and ER-PK.**

425 **Panels (b) and (d) describe the absolute differences in monthly mean ET and R_{eco} within East River Watershed between**
426 **deciduous forests, evergreen forests, meadow grasslands, and riparian shrublands.**

427 **5. Discussion**

428 Our study demonstrates that HPM provides reliable estimations of ET and R_{eco} under various climate and
429 vegetation conditions. The unique gated structures and cell states of LSTM allow HPM to track information from
430 earlier times and decide which information to pass along and which information to forget. This effective configuration
431 allows LSTM to effectively capture the long-term dependencies and ecological memory effects among meteorological
432 forcings, NDVI, ET and R_{eco} . With 70 % of the data used for training (model development), ET and R_{eco} estimation
433 from HPM achieves an average adjusted R^2 of 0.9 compared to flux tower measurements. To demonstrate HPM's
434 applicability for providing ET and R_{eco} estimation at sparsely monitored watersheds, we presented four use cases,
435 including prediction ET and R_{eco} in the time domain, data-driven HPMs and mechanistic HPMs. Results from the four
436 use cases suggest HPM is a powerful approach to estimate ET and R_{eco} at target watersheds requiring only 5 commonly
437 available input data and can advance our understanding of watershed processes.

438 HPM was capable incorporating information from NDVI time series to delineate the physiological
439 differences among deciduous forests, evergreen forests, shrublands and grasslands. In our study, NDVI data indicated
440 evergreen forests have a longer growing season compared to other vegetation types and deciduous forests have higher
441 peak NDVI values. Correspondingly, we also observed an earlier increase in ET and R_{eco} for evergreen forests (before
442 May), but larger ET and R_{eco} for deciduous forests during peak growing season (around June and July). Baldocchi et
443 al. (2010) found that deciduous forests had a shorter growing season, but showed a greater capacity for assimilating
444 carbon during the growing season. Evergreen forests, on the other hand, had an extended growing season but with a
445 smaller capacity for gaining carbon. They found older leaves tend to have smaller leaf nitrogen and stomata
446 conductance that lead to smaller ET and R_{eco} during peak growing seasons. Hu et al. (2010) found that extended
447 growing season length resulted in less annual CO_2 uptake at Niwot Ridge, USA. They found increasing growing
448 season length is usually correlated with decreasing snow water storage and decreasing forest carbon uptake. Xu et al.
449 (2020) suggested canopy photosynthetic capacity is the driving force that lead to different resources use efficiencies
450 (RUEs) between deciduous forests and evergreen forests. Novick et al. (2015) focused on the net ecosystem exchange
451 of CO_2 and also suggested seasonality is less important for evergreen forests, where significant amounts of carbon
452 were assimilated outside of active season. These findings are similar to what we found in HPM estimations, where we
453 observed a greater ET and R_{eco} contribution during early and later seasons for evergreen forests compared to deciduous
454 forests that have significantly greater peak ET and R_{eco} during peak growing season. As HPM only requires 5 input
455 features and NDVI is the only variable related with vegetation types, we were not able to perform detailed analysis
456 delineating the physiological control on ET and R_{eco} dynamics. But we believe HPM models are still useful as they
457 can be provide initial ET and R_{eco} estimation that help with site selection and field campaign designs.

458 Temporal variability in meteorological conditions also leads to unique ET and R_{eco} responses at the East
459 River Watershed, as shown by HPM estimations. Three years with a diverse combination of snow and rain
460 precipitation were analyzed. In 2012, a year that experienced earlier snowmelt, both ET and R_{eco} increased early in

461 the season. However, earlier growth in vegetation and increasing demand for water resulted in fore-summer drought
462 conditions that led to decreases in ET and R_{eco} in late May and June. In 2014, HPM estimated a steady increase in ET
463 and R_{eco} during spring months following radiation and air temperature trends, with no subsequent significant decline
464 in ET and R_{eco} . This indicates that energy was still the key limiting factor for spring dynamics in 2014, leading to a
465 smaller pre-June ET and R_{eco} compared to 2012. Following an earlier arrival of monsoon in 2012 compared to 2014
466 and 2015, we observed higher mean ET and R_{eco} in July than in June, which indicates the earlier arrival of monsoon
467 precipitation greatly reduced the moisture limiting condition caused by fore-summer drought and led to subsequent
468 increase in ET and R_{eco} . During late summer and autumn months, radiation declined significantly with $\sim 30\%$ decrease
469 in August and $\sim 40\%$ decrease in September. Though 2012, 2014 and 2015 had diverse monsoon precipitation during
470 these periods, HPM did not estimate significant differences in post-July ET. This result indicates the East River
471 watershed is mainly under energy-limiting rather than moisture-limiting conditions during late-summer and autumn;
472 and timing of monsoon arrival is more important than the absolute amount of monsoon precipitation for ET dynamics.
473 This result is consistent with findings in Carroll et al. (2020). Their study also indicated earlier arrival of summer
474 monsoon was effectively supporting ET and that the monsoon precipitation was quickly consumed by vegetation,
475 whereas later arrival of summer monsoon water mainly contributed to streamflow under energy-limiting conditions.

476 Uncertainties of HPM models arise from several aspects. First, current choices of only five input features
477 based on data availability may decrease estimation accuracy in certain environments, such as sites with seasonally dry
478 periods. Though the LSTM component within HPMs can capture the memory effects and long-term dependencies of
479 watershed dynamics, rare extreme values are difficult to be captured by LSTM due to insufficient training data for
480 such cases. For example, we observed a decreasing prediction accuracy for ET and R_{eco} estimation at sites that
481 experience drought conditions. Current use of meteorological forcings data and NDVI may not provide sufficient data
482 for LSTM to identify droughts implicitly. Other key variables (e.g., soil moisture) when available can potentially be
483 useful to help LSTM better quantify these rare events and increase model performance. Secondly, parameterization
484 and insufficient spatiotemporal resolution of meteorological data still remain a challenge. Field observations along the
485 Rocky Mountain ranges have shown that south-facing hillslopes have significantly earlier snowmelt compared to
486 north-facing hillslopes (Kampf et al., 2015; Webb et al., 2018). However, we did not observe same level of
487 heterogeneities in radiation and air temperature in reanalysis data compared to weather station data (Fig. S4 and S5).
488 Mu et al. (2013) and Zhang et al. (2019) suggested uncertainties in meteorological inputs can result in large errors
489 (i.e., $> 20\%$ MAE) and reduce accuracy by 10 – 30%. Additionally, HPM is also influenced by remote sensing inputs
490 accuracy, including but not limited to insufficient resolution, cloud conditions, spatial averaging, temporal
491 reconstruction, any other algorithms involved. But with recent advances in remote sensing and satellite technologies
492 (McCabe et al., 2017) and harmonized Landsat-Sentinel datasets (Claverie et al., 2018), the spatial and temporal
493 resolution should greatly increase in the future (i.e., 3 m resolution and daily). Finally, errors can stem from the HPM
494 hybrid approaches and conceptual model uncertainties. Any original errors in mechanistic models will be passed onto
495 HPM estimations of ET and R_{eco} . We recommend to train data-driven HPM and mechanistic HPM using long time
496 series (e.g., > 5 years) with high quality data or simulations, which enables HPMs to better memorize long-term
497 dependencies of ecosystem dynamics. Though some of the uncertainties still remain a challenge, efforts have been

498 made to minimize them through the technical advances described herein. Future HPM models can potentially be jointly
499 trained on FLUXNET and process-based simulations to bypass certain limitations and provide more accurate ET and
500 R_{eco} at sparsely monitored watersheds.

501 **6. Conclusion**

502 In this study, we developed and tested a Hybrid Predictive Modeling approach for ET and R_{eco} estimation,
503 with an enhanced focus on a watershed in the Rocky Mountains. We developed individual HPM models at various
504 FLUXNET sites and at sites where data could support the proper development of a mechanistic model (e.g., CLM).
505 These models were **trained and** validated against eddy covariance measurements and CLM outputs. We further used
506 these models for ET and R_{eco} estimation at watersheds within the same ecoregion to test HPM's capability of providing
507 estimation over space, where only meteorological forcings data and remote sensing data were available. Lastly, we
508 applied the HPM to provide long-term estimation of ET and R_{eco} and test the sensitivity of HPM to various vegetation
509 and meteorological conditions within the East River Watershed of CO, USA.

510 Given the promising results of HPM, the approach offers an avenue for estimating ET and R_{eco} using easy-
511 to-acquire or commonly available datasets. This study also suggests that the spatial heterogeneity of meteorological
512 forcings and vegetation dynamics have significant impacts on ET and R_{eco} dynamics, which may be currently
513 underestimated due to typically coarse spatial resolution of data inputs. Parameters related to energy and soil moisture
514 conditions can be implemented into HPM to increase HPM's accuracy, especially for sites in ecoregions limited by
515 soil moisture conditions. Lastly, it should be pointed out that HPM is not restricted to estimation of ET and R_{eco} only.
516 HPM also has great potential for estimating other parameters important for water and carbon cycles given the right
517 choice of input variables, such as net ecosystem exchange (Figure A6). Thus, we believe the proposed HPM model
518 can improve our prediction capabilities of ET and R_{eco} at sparsely monitored watersheds and advance our
519 understanding of watershed dynamics.

520 **Data availability.** The data used in this study are from publicly available datasets. FLUXNET measurements can be
521 accessed at <https://FLUXNET.fluxdata.org>. SNOTEL data are available at <https://www.wcc.nrcs.usda.gov/snow/>.
522 DAYMET data can be found at (Thornton et al., 2017) or via Google Earth Engine. Landsat data are available on
523 Google Earth Engine. All data and simulated results and model parameters associated with this article can be found at
524 <https://data.ess-dive.lbl.gov/view/doi:10.15485/1633810>.

525 **Acknowledgements.** This material is based upon work supported as part of the Watershed Function Scientific Focus
526 Area funded by the U.S. Department of Energy, Office of Science, Office of Biological and Environmental Research
527 under Award Number DE-AC02-05CH11231. We thank Haruko Wainwright and Bhavna Arora for providing
528 comments on East River estimations. We also greatly appreciate all the guidance provided by Professor Yoram Rubin
529 and Professor Dennis Baldocchi at UC Berkeley to the first author. We also acknowledge the Jane Lewis Fellowship
530 Committee of the UC Berkeley for providing fellowship support to the first author.

531 **References**

532 Abatzoglou, J. T., Barbero, R., Wolf, J. W. and Holden, Z. A.: Tracking Interannual Streamflow Variability with
533 Drought Indices in the U.S. Pacific Northwest, *J. Hydrometeorol.*, doi:10.1175/jhm-d-13-0167.1, 2014.

534 Ai, J., Jia, G., Epstein, H. E., Wang, H., Zhang, A. and Hu, Y.: MODIS-Based Estimates of Global Terrestrial
535 Ecosystem Respiration, *J. Geophys. Res. Biogeosciences*, 123(2), 326–352, doi:10.1002/2017JG004107, 2018.

536 Allen, R. G., Pereira, L. S., Raes, D. and Smith, M.: Crop evapotranspiration: Guidelines for computing crop
537 requirements., 1998.

538 Anderson, M. C., Allen, R. G., Morse, A. and Kustas, W. P.: Use of Landsat thermal imagery in monitoring
539 evapotranspiration and managing water resources, *Remote Sens. Environ.*, doi:10.1016/j.rse.2011.08.025, 2012.

540 Baldocchi, D.: Measuring fluxes of trace gases and energy between ecosystems and the atmosphere - the state and
541 future of the eddy covariance method, *Glob. Chang. Biol.*, doi:10.1111/gcb.12649, 2014.

542 Baldocchi, D. D., Ma, S., Rambal, S., Misson, L., Ourcival, J. M., Limousin, J. M., Pereira, J. and Papale, D.: On the
543 differential advantages of evergreenness and deciduousness in mediterranean oak woodlands: A flux perspective,
544 *Ecol. Appl.*, 20(6), 1583–1597, doi:10.1890/08-2047.1, 2010.

545 Berryman, E. M., Vanderhoof, M. K., Bradford, J. B., Hawbaker, T. J., Henne, P. D., Burns, S. P., Frank, J. M.,
546 Birdsey, R. A. and Ryan, M. G.: Estimating Soil Respiration in a Subalpine Landscape Using Point, Terrain,
547 Climate, and Greenness Data, *J. Geophys. Res. Biogeosciences*, 123(10), 3231–3249, doi:10.1029/2018JG004613,
548 2018.

549 Bodesheim, P., Jung, M., Gans, F., Mahecha, M. D. and Reichstein, M.: Upscaled diurnal cycles of land-
550 Atmosphere fluxes: A new global half-hourly data product, *Earth Syst. Sci. Data*, 10(3), 1327–1365,
551 doi:10.5194/essd-10-1327-2018, 2018.

552 Budyko, M. I.: The Heat Balance of the Earth's Surface, *Sov. Geogr.*, 2(4), 3–13,
553 doi:10.1080/00385417.1961.10770761, 1961.

554 Carroll, R. W. H., Gochis, D. and Williams, K. H.: Efficiency of the Summer Monsoon in Generating Streamflow
555 Within a Snow-Dominated Headwater Basin of the Colorado River, *Geophys. Res. Lett.*, 47(23),
556 doi:10.1029/2020GL090856, 2020.

557 Chang, L. L., Dwivedi, R., Knowles, J. F., Fang, Y. H., Niu, G. Y., Pelletier, J. D., Rasmussen, C., Durcik, M.,
558 Barron-Gafford, G. A. and Meixner, T.: Why Do Large-Scale Land Surface Models Produce a Low Ratio of
559 Transpiration to Evapotranspiration?, *J. Geophys. Res. Atmos.*, doi:10.1029/2018JD029159, 2018.

560 Chu, H., Luo, X., Ouyang, Z., Chan, W. S., Dengel, S., Biraud, S. C., Torn, M. S., Metzger, S., Kumar, J., Arain, M.
561 A., Arkebauer, T. J., Baldocchi, D., Bernacchi, C., Billesbach, D., Black, T. A., Blanken, P. D., Bohrer, G., Bracho,
562 R., Brown, S., Brunzell, N. A., Chen, J., Chen, X., Clark, K., Desai, A. R., Duman, T., Durden, D., Fares, S.,
563 Forbrich, I., Gamon, J. A., Gough, C. M., Griffis, T., Helbig, M., Hollinger, D., Humphreys, E., Ikawa, H., Iwata,
564 H., Ju, Y., Knowles, J. F., Knox, S. H., Kobayashi, H., Kolb, T., Law, B., Lee, X., Litvak, M., Liu, H., Munger, J.
565 W., Noormets, A., Novick, K., Oberbauer, S. F., Oechel, W., Oikawa, P., Papuga, S. A., Pendall, E., Prajapati, P.,
566 Prueger, J., Quinton, W. L., Richardson, A. D., Russell, E. S., Scott, R. L., Starr, G., Staebler, R., Stoy, P. C., Stuart-
567 Haëntjens, E., Sonnentag, O., Sullivan, R. C., Suyker, A., Ueyama, M., Vargas, R., Wood, J. D. and Zona, D.:
568 Representativeness of Eddy-Covariance flux footprints for areas surrounding AmeriFlux sites, *Agric. For. Meteorol.*,
569 301–302(February), doi:10.1016/j.agrformet.2021.108350, 2021.

570 Claverie, M., Ju, J., Masek, J. G., Dungan, J. L., Vermote, E. F., Roger, J. C., Skakun, S. V. and Justice, C.: The
571 Harmonized Landsat and Sentinel-2 surface reflectance data set, *Remote Sens. Environ.*,
572 doi:10.1016/j.rse.2018.09.002, 2018.

573 Cox, P. M., Betts, R. A., Jones, C. D., Spall, S. A. and Totterdell, I. J.: Acceleration of global warming due to
574 carbon-cycle feedbacks in a coupled climate model, *Nature*, doi:10.1038/35041539, 2000.

575 Daggars, T. D., Kromkamp, J. C., Herman, P. M. J. and van der Wal, D.: A model to assess microphytobenthic
576 primary production in tidal systems using satellite remote sensing, *Remote Sens. Environ.*, 211(April), 129–145,
577 doi:10.1016/j.rse.2018.03.037, 2018.

578 Falco, N., Wainwright, H., Dafflon, B., Léger, E., Peterson, J., Steltzer, H., Wilmer, C., Rowland, J. C., Williams, K.
579 H. and Hubbard, S. S.: Investigating Microtopographic and Soil Controls on a Mountainous Meadow Plant
580 Community Using High-Resolution Remote Sensing and Surface Geophysical Data, *J. Geophys. Res.*
581 *Biogeosciences*, doi:10.1029/2018JG004394, 2019.

582 Gao, X., Mei, X., Gu, F., Hao, W., Li, H. and Gong, D.: Ecosystem respiration and its components in a rainfed
583 spring maize cropland in the Loess Plateau, China, *Sci. Rep.*, doi:10.1038/s41598-017-17866-1, 2017.

584 Gao, Y., Yu, G., Li, S., Yan, H., Zhu, X., Wang, Q., Shi, P., Zhao, L., Li, Y., Zhang, F., Wang, Y. and Zhang, J.: A
585 remote sensing model to estimate ecosystem respiration in Northern China and the Tibetan Plateau, *Ecol. Modell.*,
586 doi:10.1016/j.ecolmodel.2015.03.001, 2015.

587 van Gorsel, E., Delpierre, N., Leuning, R., Black, A., Munger, J. W., Wofsy, S., Aubinet, M., Feigenwinter, C.,
588 Beringer, J., Bonal, D., Chen, B., Chen, J., Clement, R., Davis, K. J., Desai, A. R., Dragoni, D., Etzold, S.,
589 Grünwald, T., Gu, L., Heinesch, B., Hutrya, L. R., Jans, W. W. P., Kutsch, W., Law, B. E., Leclerc, M. Y.,
590 Mammarella, I., Montagnani, L., Noormets, A., Rebmann, C. and Wharton, S.: Estimating nocturnal ecosystem
591 respiration from the vertical turbulent flux and change in storage of CO₂, *Agric. For. Meteorol.*, 149(11), 1919–
592 1930, doi:10.1016/j.agrformet.2009.06.020, 2009.

593 Greve, P., Gudmundsson, L., Orlowsky, B. and Seneviratne, S. I.: Introducing a probabilistic Budyko framework,
594 *Geophys. Res. Lett.*, 42(7), 2261–2269, doi:10.1002/2015GL063449, 2015.

595 Hargrove, W. W. and Hoffman, F. M.: Using multivariate clustering to characterize ecoregion borders, *Comput. Sci.*
596 *Eng.*, 1(4), 18–25, doi:10.1109/5992.774837, 1999.

597 Hargrove, W. W., Hoffman, F. M. and Law, B. E.: New analysis reveals representativeness of the amerflux network,
598 *Eos (Washington, DC.)*, 84(48), doi:10.1029/2003EO480001, 2003.

599 Hochreiter, S. and Schmidhuber, J.: Long Short-Term Memory, *Neural Comput.*, doi:10.1162/neco.1997.9.8.1735,
600 1997.

601 Homer, C., Dewitz, J., Yang, L., Jin, S., Danielson, P., Xian, G., Coulston, J., Herold, N., Wickham, J. and Megown,
602 K.: Completion of the 2011 national land cover database for the conterminous United States – Representing a
603 decade of land cover change information, *Photogramm. Eng. Remote Sensing*, doi:10.1016/S0099-1112(15)30100-
604 2, 2015.

605 Hu, J., Moore, D. J. P., Burns, S. P. and Monson, R.: Longer growing seasons lead to less carbon sequestration by a
606 subalpine forest, *Glob. Chang. Biol.*, 16(2), 771–783, doi:10.1111/j.1365-2486.2009.01967.x, 2010.

607 Hubbard, S. S., Williams, K. H., Agarwal, D., Banfield, J., Beller, H., Bouskill, N., Brodie, E., Carroll, R., Dafflon,
608 B., Dwivedi, D., Falco, N., Faybishenko, B., Maxwell, R., Nico, P., Steefel, C., Steltzer, H., Tokunaga, T., Tran, P.
609 A., Wainwright, H. and Varadharajan, C.: The East River, Colorado, Watershed: A Mountainous Community
610 Testbed for Improving Predictive Understanding of Multiscale Hydrological–Biogeochemical Dynamics, *Vadose*
611 *Zo. J.*, 17(1), 0, doi:10.2136/vzj2018.03.0061, 2018.

612 IPCC: IPCC 2019- Special report on climate change, desertification, land degradation, sustainable land
613 management, food security, and greenhouse gas fluxes in terrestrial ecosystem, *Res. Handb. Clim. Chang. Agric.*
614 *Law*, doi:10.4337/9781784710644, 2019.

615 Irons, J. R., Dwyer, J. L. and Barsi, J. A.: The next Landsat satellite: The Landsat Data Continuity Mission, *Remote*
616 *Sens. Environ.*, doi:10.1016/j.rse.2011.08.026, 2012.

617 Jägermeyr, J., Gerten, D., Lucht, W., Hostert, P., Migliavacca, M. and Nemani, R.: A high-resolution approach to
618 estimating ecosystem respiration at continental scales using operational satellite data, *Glob. Chang. Biol.*,
619 doi:10.1111/gcb.12443, 2014.

620 Jung, M., Reichstein, M., Ciais, P., Seneviratne, S. I., Sheffield, J., Goulden, M. L., Bonan, G., Cescatti, A., Chen,
621 J., De Jeu, R., Dolman, A. J., Eugster, W., Gerten, D., Gianelle, D., Gobron, N., Heinke, J., Kimball, J., Law, B. E.,
622 Montagnani, L., Mu, Q., Mueller, B., Oleson, K., Papale, D., Richardson, A. D., Rouspard, O., Running, S.,
623 Tomelleri, E., Viovy, N., Weber, U., Williams, C., Wood, E., Zaehle, S. and Zhang, K.: Recent decline in the global

- 624 land evapotranspiration trend due to limited moisture supply, *Nature*, doi:10.1038/nature09396, 2010.
- 625 Jung, M., Reichstein, M., Schwalm, C. R., Huntingford, C., Sitch, S., Ahlström, A., Arneth, A., Camps-Valls, G.,
626 Ciais, P., Friedlingstein, P., Gans, F., Ichii, K., Jain, A. K., Kato, E., Papale, D., Poulter, B., Raduly, B., Rödenbeck,
627 C., Tramontana, G., Viovy, N., Wang, Y. P., Weber, U., Zaehle, S. and Zeng, N.: Compensatory water effects link
628 yearly global land CO₂ sink changes to temperature, *Nature*, 541(7638), 516–520, doi:10.1038/nature20780, 2017.
- 629 Kakalia, Z., Varadharajan, C., Alper, E., Brodie, E., Burrus, M., Carroll, R., Christianson, D., Hendrix, V.,
630 Henderson, M., Hubbard, S., Johnson, D., Versteeg, R., Williams, K. and Agarwal, D.: The East River Community
631 Observatory Data Collection: Diverse, multiscale data from a mountainous watershed in the East River, Colorado, ,
632 1–17 [online] Available from: <https://doi.org/10.22541/au.160157556.64095872>, 2020.
- 633 Kampf, S., Markus, J., Heath, J. and Moore, C.: Snowmelt runoff and soil moisture dynamics on steep subalpine
634 hillslopes, *Hydrol. Process.*, 29(5), 712–723, doi:10.1002/hyp.10179, 2015.
- 635 Keenan, T. F., Migliavacca, M., Papale, D., Baldocchi, D., Reichstein, M., Torn, M. and Wutzler, T.: Widespread
636 inhibition of daytime ecosystem respiration, *Nat. Ecol. Evol.*, 3(3), 407–415, doi:10.1038/s41559-019-0809-2, 2019.
- 637 Knowles, J. F., Blanken, P. D. and Williams, M. W.: Wet meadow ecosystems contribute the majority of overwinter
638 soil respiration from snow-scoured alpine tundra, *J. Geophys. Res. G Biogeosciences*, 121(4), 1118–1130,
639 doi:10.1002/2015JG003081, 2016.
- 640 Kratzert, F., Klotz, D., Brenner, C., Schulz, K. and Herrnegger, M.: Rainfall–runoff modelling using Long Short-
641 Term Memory (LSTM) networks, *Hydrol. Earth Syst. Sci.*, 22(11), 6005–6022, doi:10.5194/hess-22-6005-2018,
642 2018.
- 643 Lasslop, G., Reichstein, M., Papale, D., Richardson, A., Arneth, A., Barr, A., Stoy, P. and Wohlfahrt, G.: Separation
644 of net ecosystem exchange into assimilation and respiration using a light response curve approach: Critical issues
645 and global evaluation, *Glob. Chang. Biol.*, 16(1), 187–208, doi:10.1111/j.1365-2486.2009.02041.x, 2010.
- 646 Livingston, G. P. and Hutchinson, G. L.: Enclosure-based measurement of trace gas exchange: applications and
647 sources of error., 1995.
- 648 Ma, Y., Liu, S., Song, L., Xu, Z., Liu, Y., Xu, T. and Zhu, Z.: Estimation of daily evapotranspiration and irrigation
649 water efficiency at a Landsat-like scale for an arid irrigation area using multi-source remote sensing data, *Remote
650 Sens. Environ.*, 216(August), 715–734, doi:10.1016/j.rse.2018.07.019, 2018.
- 651 Main-Knorn, M., Pflug, B., Louis, J., Debaecker, V., Müller-Wilm, U. and Gascon, F.: Sen2Cor for Sentinel-2.,
652 2017.
- 653 McCabe, M. F., Aragon, B., Houborg, R. and Mascaro, J.: CubeSats in Hydrology: Ultrahigh-Resolution Insights
654 Into Vegetation Dynamics and Terrestrial Evaporation, *Water Resour. Res.*, 53(12), 10017–10024,
655 doi:10.1002/2017WR022240, 2017.
- 656 Metzger, S., Junkermann, W., Mauder, M., Butterbach-Bahl, K., Trancón Y Widemann, B., Neidl, F., Schäfer, K.,
657 Wieneke, S., Zheng, X. H., Schmid, H. P. and Foken, T.: Spatially explicit regionalization of airborne flux
658 measurements using environmental response functions, *Biogeosciences*, 10(4), 2193–2217, doi:10.5194/bg-10-
659 2193-2013, 2013.
- 660 Migliavacca, M., Reichstein, M., Richardson, A. D., Mahecha, M. D., Cremonese, E., Delpierre, N., Galvagno, M.,
661 Law, B. E., Wohlfahrt, G., Andrew Black, T., Carvalhais, N., Ceccherini, G., Chen, J., Gobron, N., Koffi, E.,
662 William Munger, J., Perez-Priego, O., Robustelli, M., Tomelleri, E. and Cescatti, A.: Influence of physiological
663 phenology on the seasonal pattern of ecosystem respiration in deciduous forests, *Glob. Chang. Biol.*, 21(1), 363–
664 376, doi:10.1111/gcb.12671, 2015.
- 665 Mohanty, B. P., Cosh, M. H., Lakshmi, V. and Montzka, C.: Soil moisture remote sensing: State-of-the-science,
666 *Vadose Zo. J.*, doi:10.2136/vzj2016.10.0105, 2017.
- 667 Mu, Q., Zhao, M. and Running, S. W.: MODIS Global Terrestrial Evapotranspiration (ET) Product
668 (MOD16A2/A3), Algorithm Theor. Basis Doc., 2013.

- 669 NASA: Moderate Resolution Imaging Spectroradiometer (MODIS) Overview, Nasa, 2008.
- 670 Novick, K. A., Oishi, A. C., Ward, E. J., Siqueira, M. B. S., Juang, J. Y. and Stoy, P. C.: On the difference in the net
671 ecosystem exchange of CO₂ between deciduous and evergreen forests in the southeastern United States, *Glob.*
672 *Chang. Biol.*, 21(2), doi:10.1111/gcb.12723, 2015.
- 673 Olah, C.: Understanding LSTM Networks, <https://colah.github.io/posts/2015-08-Understanding-LSTMs/>, 2015,
674 2015.
- 675 Oleson, K. W., Lawrence, D. M., Bonan, G. B., Drewniak, B., Huang, M., Koven, C. D., Levis, S., Li, F., Riley, J.,
676 Subin, Z. M., Swenson, S. C., Thornton, P. E., Bozbiyik, A., Fisher, R. A., Heald, C. L., Kluzek, E., Lamarque, J.-
677 F., Lawrence, P. J., Leung, L. R., Lipscomb, W., Muszala, S., Ricciuto, D. M., Sacks, W. J., Sun, Y., Tang, J. and
678 Yang, Z.-L.: Technical Description of version 4.5 of the Community Land Model (CLM), 2013.
- 679 Omernik, J. M.: Perspectives on the nature and definition of ecological regions., *Environ. Manage.*,
680 doi:10.1007/s00267-003-5197-2, 2004.
- 681 Omernik, J. M. and Griffith, G. E.: Ecoregions of the Conterminous United States: Evolution of a Hierarchical
682 Spatial Framework, *Environ. Manage.*, doi:10.1007/s00267-014-0364-1, 2014.
- 683 Oyler, J. W., Dobrowski, S. Z., Ballantyne, A. P., Klene, A. E. and Running, S. W.: Artificial amplification of
684 warming trends across the mountains of the western United States, *Geophys. Res. Lett.*,
685 doi:10.1002/2014GL062803, 2015.
- 686 Paca, V. H. da M., Espinoza-Dávalos, G. E., Hessels, T. M., Moreira, D. M., Comair, G. F. and Bastiaanssen, W. G.
687 M.: The spatial variability of actual evapotranspiration across the Amazon River Basin based on remote sensing
688 products validated with flux towers, *Ecol. Process.*, 8(1), doi:10.1186/s13717-019-0158-8, 2019.
- 689 Priestley, C. H. B. and Taylor, R. J.: On the Assessment of Surface Heat Flux and Evaporation Using Large-Scale
690 Parameters, *Mon. Weather Rev.*, doi:10.1175/1520-0493(1972)100<0081:otaosh>2.3.co;2, 1972.
- 691 Pumpanen, J., Kolari, P., Ilvesniemi, H., Minkinen, K., Vesala, T., Niinistö, S., Lohila, A., Larmola, T., Morero,
692 M., Pihlatie, M., Janssens, I., Yuste, J. C., Grünzweig, J. M., Reth, S., Subke, J. A., Savage, K., Kutsch, W.,
693 Østreg, G., Ziegler, W., Anthoni, P., Lindroth, A. and Hari, P.: Comparison of different chamber techniques for
694 measuring soil CO₂ efflux, *Agric. For. Meteorol.*, doi:10.1016/j.agrformet.2003.12.001, 2004.
- 695 Reichstein, M., Falge, E., Baldocchi, D., Papale, D., Aubinet, M., Berbigier, P., Bernhofer, C., Buchmann, N.,
696 Gilmanov, T., Granier, A., Grünwald, T., Havránková, K., Ilvesniemi, H., Janous, D., Knohl, A., Laurila, T., Lohila,
697 A., Loustau, D., Matteucci, G., Meyers, T., Miglietta, F., Ourcival, J. M., Pumpanen, J., Rambal, S., Rotenberg, E.,
698 Sanz, M., Tenhunen, J., Seufert, G., Vaccari, F., Vesala, T., Yakir, D. and Valentini, R.: On the separation of net
699 ecosystem exchange into assimilation and ecosystem respiration: Review and improved algorithm, *Glob. Chang.*
700 *Biol.*, doi:10.1111/j.1365-2486.2005.001002.x, 2005.
- 701 Reichstein, M., Camps-Valls, G., Stevens, B., Jung, M., Denzler, J., Carvalhais, N. and Prabhat: Deep learning and
702 process understanding for data-driven Earth system science, *Nature*, 566(7743), 195–204, doi:10.1038/s41586-019-
703 0912-1, 2019.
- 704 Ren, H., Cromwell, E., Kravitz, B. and Chen, X.: Using Deep Learning to Fill Spatio-Temporal Data Gaps in
705 Hydrological Monitoring Networks, *Hydrol. Earth Syst. Sci. Discuss.*, (May), 1–20, doi:10.5194/hess-2019-196,
706 2019.
- 707 Rungee, J., Bales, R. and Goulden, M.: Evapotranspiration response to multiyear dry periods in the semiarid western
708 United States, *Hydrol. Process.*, doi:10.1002/hyp.13322, 2019.
- 709 Ryu, Y., Baldocchi, D. D., Kobayashi, H., Van Ingen, C., Li, J., Black, T. A., Beringer, J., Van Gorsel, E., Knohl,
710 A., Law, B. E. and Rouspard, O.: Integration of MODIS land and atmosphere products with a coupled-process
711 model to estimate gross primary productivity and evapotranspiration from 1 km to global scales, *Global*
712 *Biogeochem. Cycles*, 25(4), 1–24, doi:10.1029/2011GB004053, 2011.
- 713 Seneviratne, S. I., Lüthi, D., Litschi, M. and Schär, C.: Land-atmosphere coupling and climate change in Europe,

714 Nature, doi:10.1038/nature05095, 2006.

715 Strachan, S., Kelsey, E. P., Brown, R. F., Dascalu, S., Harris, F., Kent, G., Lyles, B., McCurdy, G., Slater, D. and
716 Smith, K.: Filling the Data Gaps in Mountain Climate Observatories Through Advanced Technology, Refined
717 Instrument Siting, and a Focus on Gradients, *Mt. Res. Dev.*, 36(4), 518–527, doi:10.1659/mrd-journal-d-16-00028.1,
718 2016.

719 Suleau, M., Moureaux, C., Dufranne, D., Buysse, P., Bodson, B., Destain, J. P., Heinesch, B., Debacq, A. and
720 Aubinet, M.: Respiration of three Belgian crops: Partitioning of total ecosystem respiration in its heterotrophic,
721 above- and below-ground autotrophic components, *Agric. For. Meteorol.*, doi:10.1016/j.agrformet.2011.01.012,
722 2011.

723 Teuling, A. J., Van Loon, A. F., Seneviratne, S. I., Lehner, I., Aubinet, M., Heinesch, B., Bernhofer, C., Grünwald,
724 T., Prasse, H. and Spank, U.: Evapotranspiration amplifies European summer drought, *Geophys. Res. Lett.*,
725 doi:10.1002/grl.50495, 2013.

726 Thornton, P. E., Thornton, M. M., Mayer, B. W., Wei, Y., Devarakonda, R., Vose, R. S. and Cook, R. B.: Daymet:
727 Daily Surface Weather Data on a 1-km Grid for North America, Version 3, ORNL DAAC, Oak Ridge, Tennessee,
728 USA, 2017.

729 Tran, A. P., Rungee, J., Faybishenko, B., Dafflon, B. and Hubbard, S. S.: Assessment of spatiotemporal variability
730 of evapotranspiration and its governing factors in a mountainous watershed, *Water (Switzerland)*, 11(2),
731 doi:10.3390/w11020243, 2019.

732 U.S. Environmental Protection Agency: Level III Ecoregions of the Continental United States, *Environ. Prot.*, 2003.

733 Visser, A., Thaw, M., Deinhart, A., Bibby, R., Safeeq, M., Conklin, M., Esser, B. and Van der Velde, Y.:
734 Cosmogenic Isotopes Unravel the Hydrochronology and Water Storage Dynamics of the Southern Sierra Critical
735 Zone, *Water Resour. Res.*, doi:10.1029/2018WR023665, 2019.

736 Viviroli, D. and Weingartner, R.: “Water towers”—A global view of the hydrological importance of mountains, in
737 *Advances in Global Change Research.*, 2008.

738 Viviroli, D., Dürr, H. H., Messerli, B., Meybeck, M. and Weingartner, R.: Mountains of the world, water towers for
739 humanity: Typology, mapping, and global significance, *Water Resour. Res.*, 43(7), 1–13,
740 doi:10.1029/2006WR005653, 2007.

741 Vogelmann, J. E., Howard, S. M., Yang, L., Larson, C. R., Wylie, B. K. and Van Driel, N.: Completion of the 1990s
742 National Land Cover Data set for the conterminous United States from Landsat thematic mapper data and ancillary
743 data sources, *Photogramm. Eng. Remote Sensing*, 2001.

744 Webb, R. W., Fassnacht, S. R. and Gooseff, M. N.: Hydrologic flow path development varies by aspect during
745 spring snowmelt in complex subalpine terrain, *Cryosphere*, 12(1), 287–300, doi:10.5194/tc-12-287-2018, 2018.

746 Wieder, W. R., Knowles, J. F., Blanken, P. D., Swenson, S. C. and Suding, K. N.: Ecosystem function in complex
747 mountain terrain: Combining models and long-term observations to advance process-based understanding, *J.*
748 *Geophys. Res. Biogeosciences*, doi:10.1002/2016JG003704, 2017.

749 Williams, M., Richardson, A. D., Reichstein, M., Stoy, P. C., Peylin, P., Verbeeck, H., Carvalhais, N., Jung, M.,
750 Hollinger, D. Y., Kattge, J., Leuning, R., Luo, Y., Tomelleri, E., Trudinger, C. and Wang, Y.-P.: Improving land
751 surface models with FLUXNET data, *Biogeosciences Discuss.*, doi:10.5194/bgd-6-2785-2009, 2009.

752 Wilson, K. B., Hanson, P. J., Mulholland, P. J., Baldocchi, D. D. and Wullschleger, S. D.: A comparison of methods
753 for determining forest evapotranspiration and its components: Sap-flow, soil water budget, eddy covariance and
754 catchment water balance, *Agric. For. Meteorol.*, 106(2), 153–168, doi:10.1016/S0168-1923(00)00199-4, 2001.

755 Xiao, J., Ollinger, S. V., Frohling, S., Hurtt, G. C., Hollinger, D. Y., Davis, K. J., Pan, Y., Zhang, X., Deng, F.,
756 Chen, J., Baldocchi, D. D., Law, B. E., Arain, M. A., Desai, A. R., Richardson, A. D., Sun, G., Amiro, B., Margolis,
757 H., Gu, L., Scott, R. L., Blanken, P. D. and Suyker, A. E.: Data-driven diagnostics of terrestrial carbon dynamics
758 over North America, *Agric. For. Meteorol.*, doi:10.1016/j.agrformet.2014.06.013, 2014.

759 Xu, H., Xiao, J., Zhang, Z., Ollinger, S. V., Hollinger, D. Y., Pan, Y. and Wan, J.: Canopy photosynthetic capacity
760 drives contrasting age dynamics of resource use efficiencies between mature temperate evergreen and deciduous
761 forests, *Glob. Chang. Biol.*, 26(11), doi:10.1111/gcb.15312, 2020.

762 Xu, L., Baldocchi, D. D. and Tang, J.: How soil moisture, rain pulses, and growth alter the response of ecosystem
763 respiration to temperature, *Global Biogeochem. Cycles*, 18(4), 1–10, doi:10.1029/2004GB002281, 2004.

764 Xu, T., Guo, Z., Liu, S., He, X., Meng, Y., Xu, Z., Xia, Y., Xiao, J., Zhang, Y., Ma, Y. and Song, L.: Evaluating
765 Different Machine Learning Methods for Upscaling Evapotranspiration from Flux Towers to the Regional Scale, *J.*
766 *Geophys. Res. Atmos.*, 123(16), 8674–8690, doi:10.1029/2018JD028447, 2018.

767 Zhang, L., Potter, N., Hickel, K., Zhang, Y. and Shao, Q.: Water balance modeling over variable time scales based
768 on the Budyko framework - Model development and testing, *J. Hydrol.*, 360(1–4), 117–131,
769 doi:10.1016/j.jhydrol.2008.07.021, 2008.

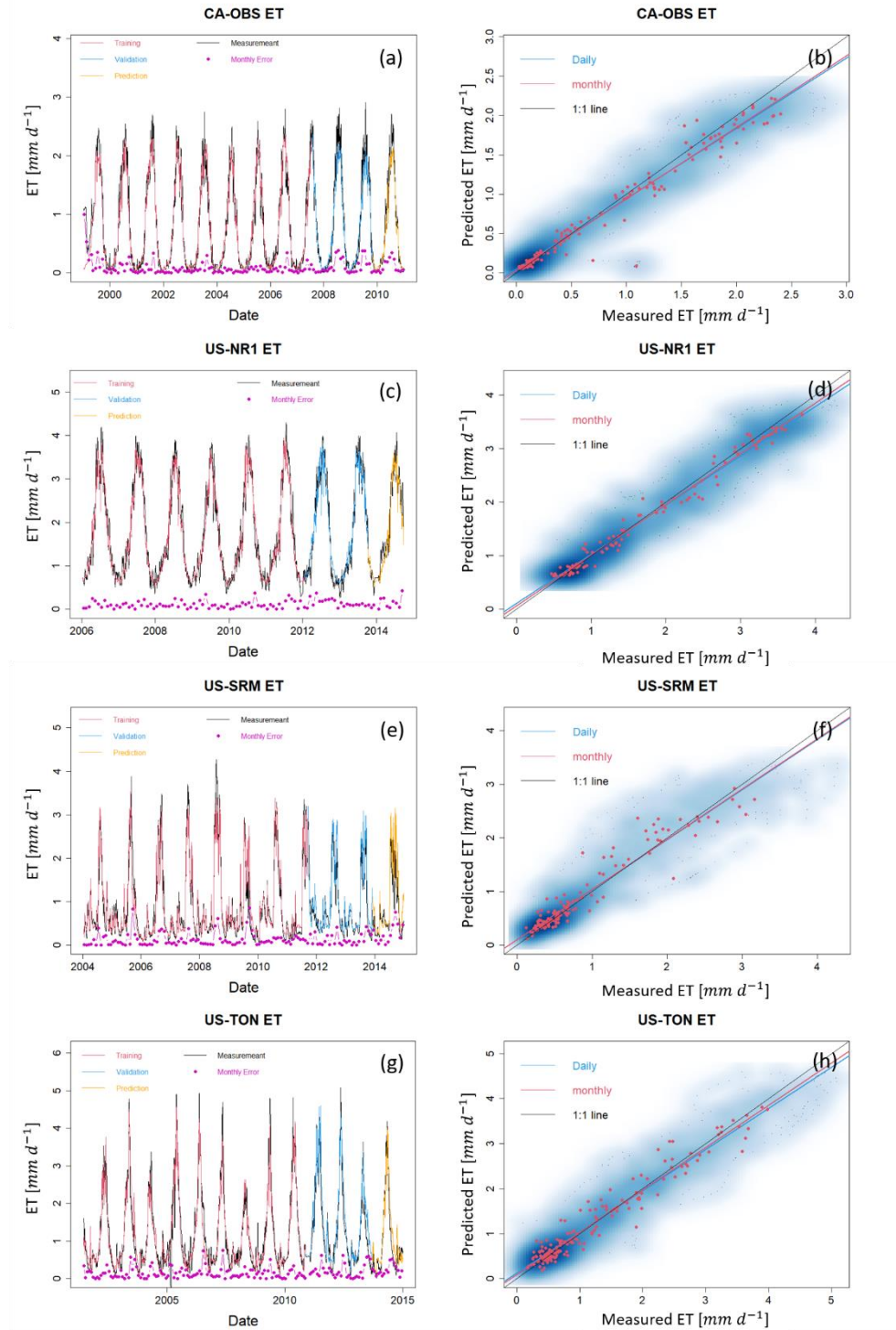
770 Zhang, Y., Kong, D., Gan, R., Chiew, F. H. S., McVicar, T. R., Zhang, Q. and Yang, Y.: Coupled estimation of
771 500 m and 8-day resolution global evapotranspiration and gross primary production in 2002–2017, *Remote Sens.*
772 *Environ.*, 222(May 2018), 165–182, doi:10.1016/j.rse.2018.12.031, 2019.

773

774 **Appendix**

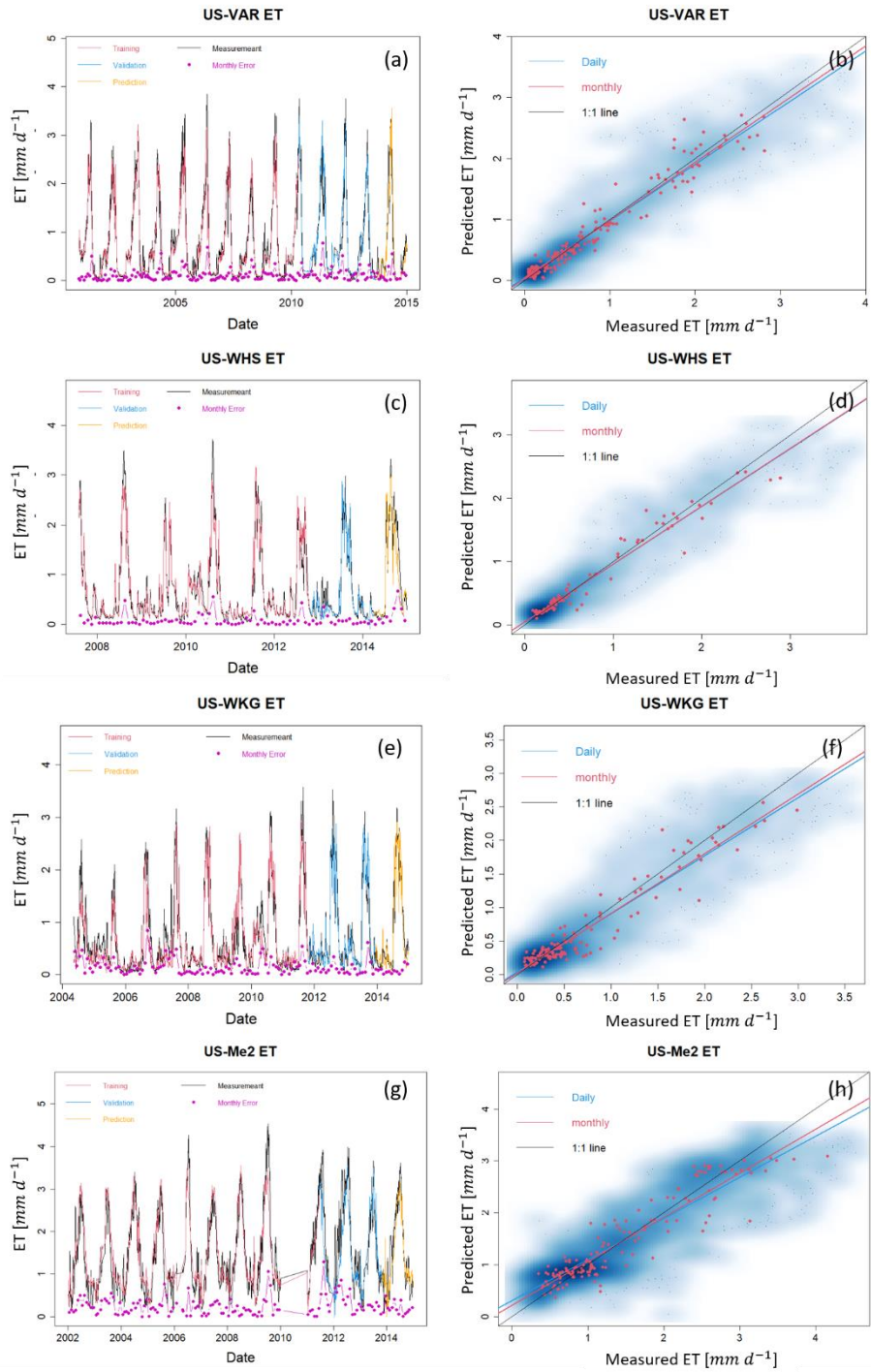
775

776 **1. ET and R_{ECO} Estimation over Time at other Fluxnet sites**



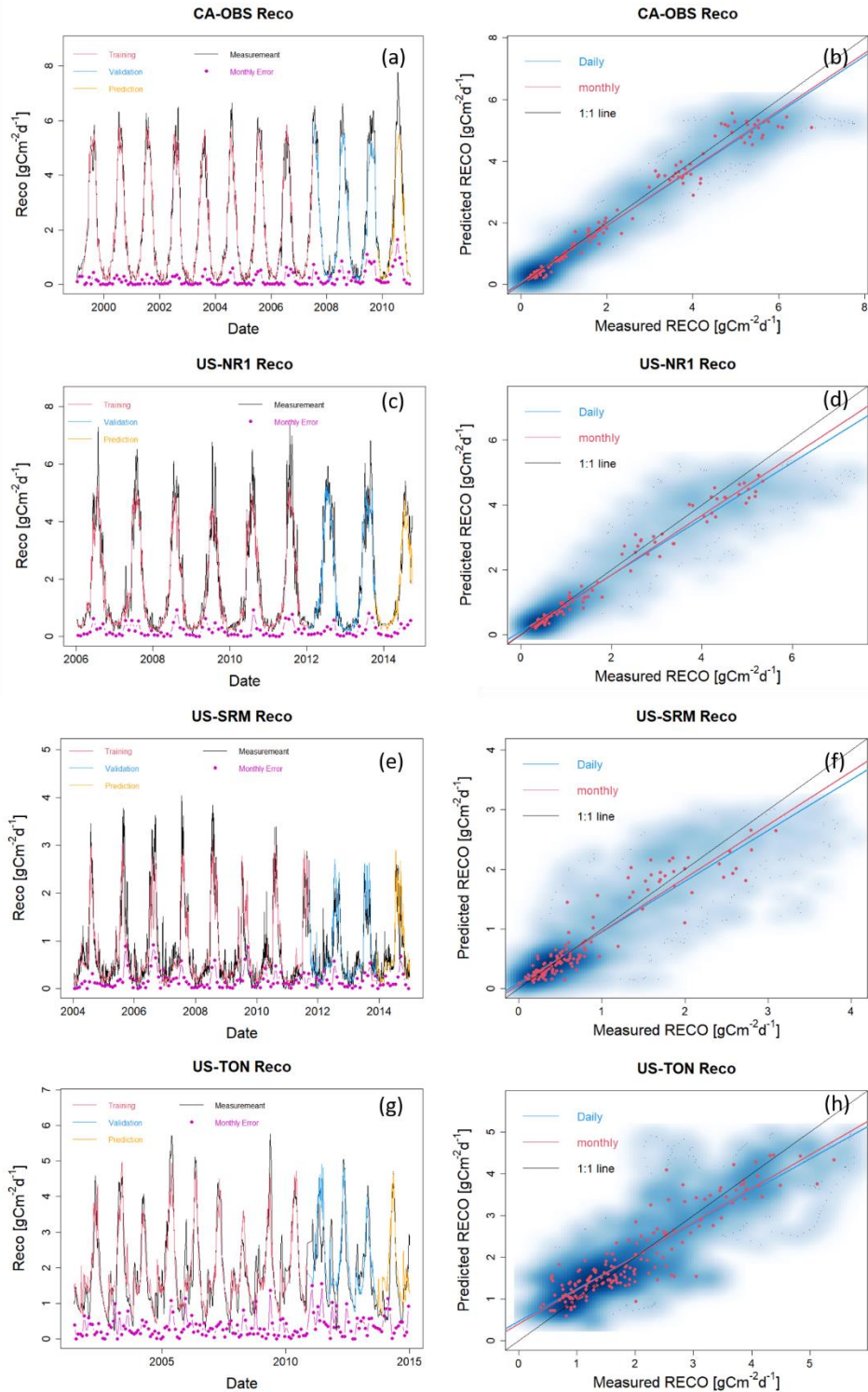
777

778 **Figure A1: ET estimation with data from selected FLUXNET sites at CA-OBS, US-NR1, US-SRM, and US-Ton. Panels (a),**
 779 **(c), (e) and (g) present daily estimations of ET separated for training, validation, and prediction. Pink points depict monthly**
 780 **error between HPM estimation and FLUXNET data. Panels (b), (d), (f) and (h) show the scatter plots of daily (blue) and**
 781 **monthly (red) ET. Darker blue clouds represent greater density of data points.**



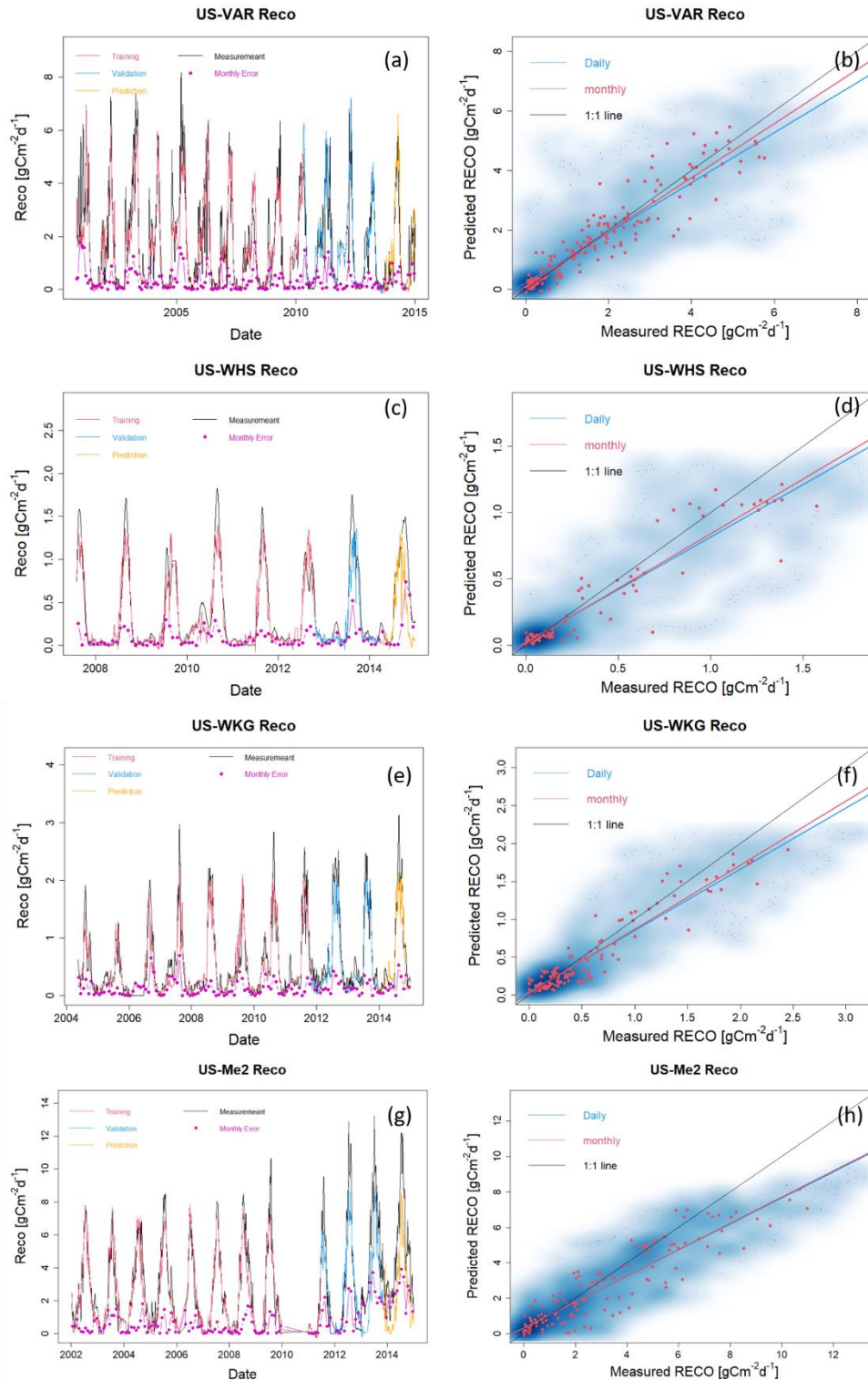
782

783 **Figure A2: ET estimation with data from selected FLUXNET sites at US-Var, US-Whs, US-Wkg and US-Me2. Panels (a),**
 784 **(c), (e) and (g) present daily estimations of ET separated for training, validation, and prediction. Pink points depict monthly**
 785 **error between HPM estimation and FLUXNET data. Panels (b), (d), (f) and (h) show the scatter plots of daily (blue) and**
 786 **monthly (red) ET. Darker blue clouds represent greater density of data points.**



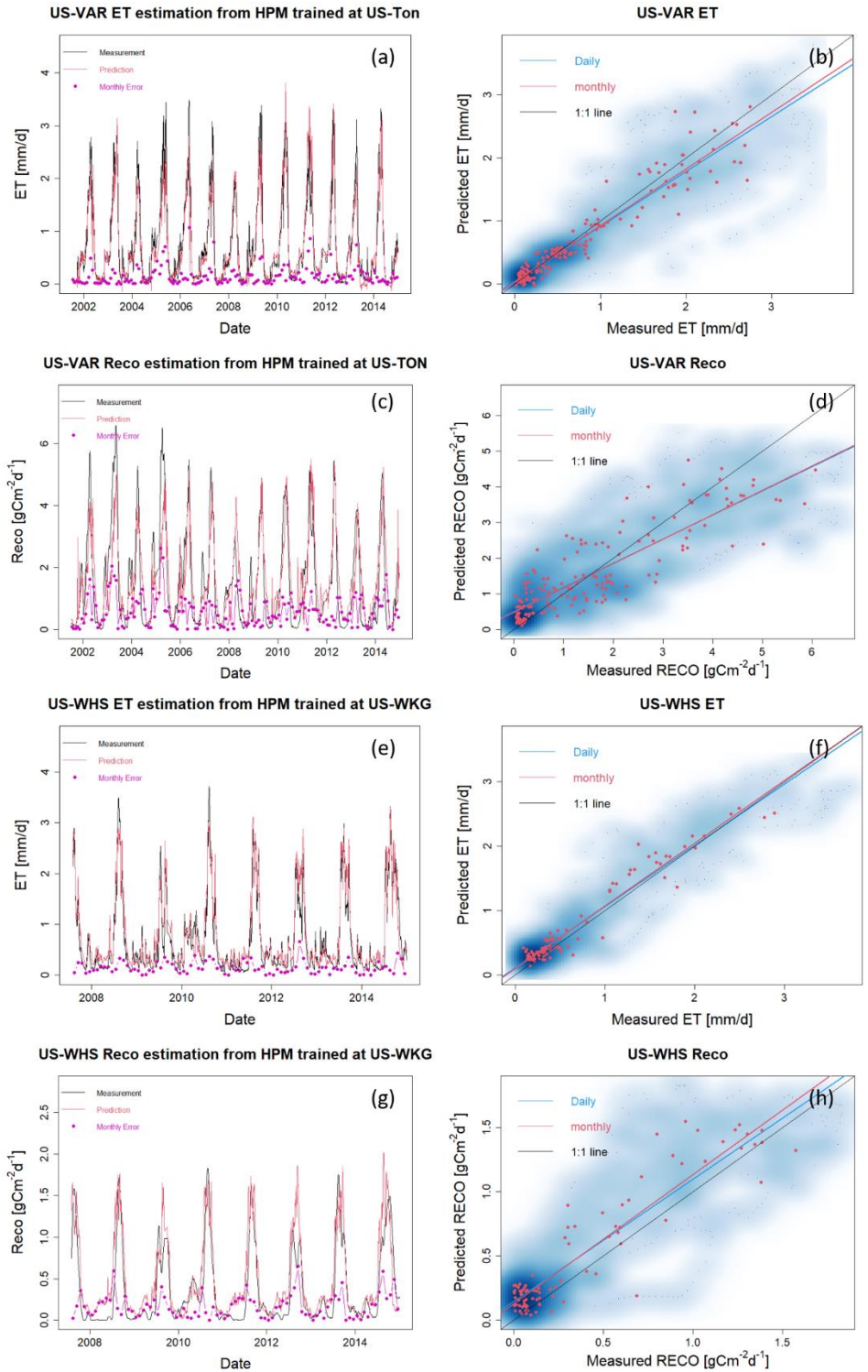
787

788 **Figure A3: R_{eco} estimation with data from selected FLUXNET sites at CA-OBS, US-NR1, US-SRM, and US-Ton. Panels**
 789 **(a), (c), (e) and (g) present daily estimations of R_{eco} separated for training, validation, and prediction. Pink points depict**
 790 **monthly error between HPM estimation and FLUXNET data. Panels (b), (d), (f) and (h) show the scatter plots of daily (blue)**
 791 **and monthly (red) R_{eco} . Darker blue clouds represent greater density of data points.**



792

793 **Figure A4: R_{eco} estimation with data from selected FLUXNET sites at US-Var, US-Whs, US-Wkg and US-Me2. Panels (a),**
 794 **(c), (e) and (g) present daily estimations of R_{eco} separated for training, validation, and prediction. Pink points depict monthly**
 795 **error between HPM estimation and FLUXNET data. Panels (b), (d), (f) and (h) show the scatter plots of daily (blue) and**
 796 **monthly (red) R_{eco} . Darker blue clouds represent greater density of data points.**



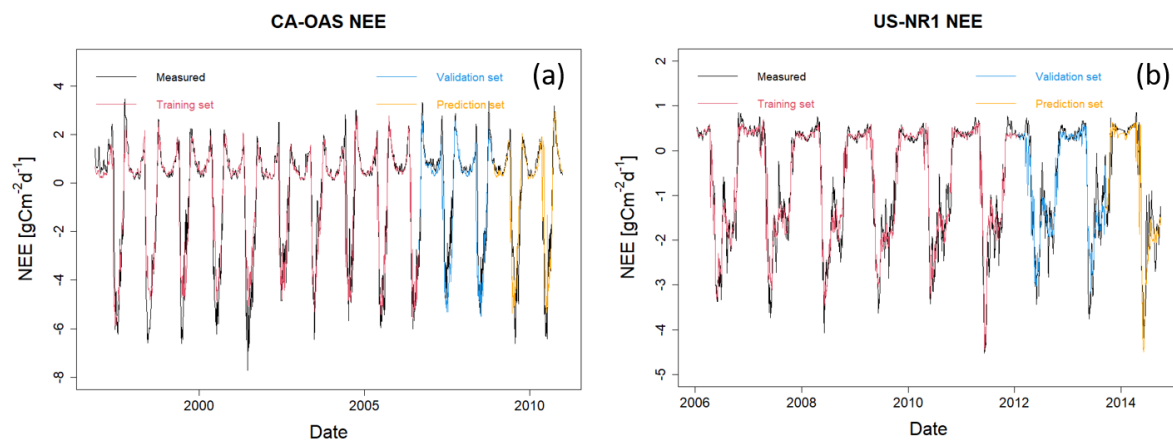
797

798

799 **Figure A5: Use case 2. ET and R_{eco} estimation at US-Var and US-Whs from HPM trained at US-Ton and US-Wky,**
 800 **respectively.**

801

802 **2. Tested NEE Estimation over Time at CA-OAS and US-NR1**



803

804 **Figure A6. HPM estimate of NEE at CA-OAS and US-NR1. R^2 between estimation and measurements are 0.87, 0.83 and**
805 **0.81 at CA-OAS; 0.94, 0.88 and 0.90 at US-NR1 for the training set, validation set and prediction set, respectively. Model**
806 **inputs include air temperature, soil temperature, sn, precipitation and radiation.**

807

808